Scatterometer Science for Future Ocean Vector Winds Missions

A White Paper

Editor:

Ernesto Rodríguez
Jet Propulsion Laboratory
California Institute of Technology

Acknowledgtements

This work was conducted by the Jet Propulsion Laboratory, California Institute of Technology, under contract with the National Aeronautics and Space Administration (NASA). We would like to thank Dr. Anthony Freeman, JPL, for organizing the ERM scatterometer science workshop and to Dr. Dudley Chelton for organizing the science agenda for the workshop.

Contents

One

Introduction

This white paper examines scientific objectives and mission options for a potential next-generation science-driven Ocean Vector Wind (OVW) scatterometer. The goal of this white paper is not to provide specific instrument or mission recommendations. Rather, we present a range of science questions that would advance NASA's Earth science goals and that go beyond the science questions driving current scatterometer missions. The implementation, technical feasibility, cost, or risk of implementing a mission to meet these goals are also beyond the scope of this white paper.

The scientific objectives for this mission have three sources: 1) the National Research Council Decadal Review recommendations for the XOVWM instrument (National Research Council, 2007); 2) the ocean vector wind community paper written for OceanObs 2009 (Bourassa et al., 2010); 3) the results of an invited meeting held at the Jet Propulsion Laboratory in January 2012 to examine science possibilities for a next-generation scatterometer mission. Although an attempt has been made to include the community consensus expressed by the NRC Decadal Review and the OceanObs community paper, the specific science goals presented in this white paper specifically attempted to match the science requirements to the expected scope and budget of a potential next-generation scatterometer mission that takes into account potential modest evolution in technology from the QuikSCAT mission. Thus, the goals presented here are from a limited science team, mindful of the community consensus, and have not yet received endorsement from the NASA Ocean Vector Winds Science Team (OVWST).

The outline of this paper is as follows: In the next sections, we present a set of themes and science questions that we have taken as a guide for the design of the next-generation scatterometer mission. Section 3 provides a detailed scientific justification for the selection of these questions and presents potential scientific benefits to be expected from such a scatterometer mission. Section 4 discusses complimentary measurements from other spaceborne sensors that could enhance the scientific value of a next-generation scatterometer mission.

The intent of this draft of this white paper is to serve as a spring-board for larger community input. The hope is that the final white paper will be a useful document for outlining science-driven options for the next-generation scatterometer. It is recognized that the current draft is limited in its coverage of all the science issues that might be impacted by such a system, and the community at large, and particularly the International Ocean Vector Winds Science Team, is encouraged to contribute towards making this a better document.

Two

Science Themes and Questions

In this section, we summarize the overarching science themes and questions for the proposed scatterometer missions, while in the next section we provide the scientific background that motivates these questions. We consider that the basic requirement of a new scatterometer mission is to contribute to the continuation of the Ocean Vector Winds (OVW) climate data record and to complement the international scatterometer constellation by providing improved temporal sampling or cross-calibration. Improvements in temporal sampling will also enable the understanding of sub-diurnal wind variations, which are interesting in themselves and need to be understood to reconcile the global OVW climate record. In addition, we point out the large scientific benefits that would result from an improvement in the spatial resolution of scatterometer winds. While increased resolution is not a minimum requirement for a future NASA scatterometer mission, it should be considered as a mission goal, if it can be implemented within the budget available to NASA for the Earth Radar Mission scatterometer option.

2.1 Decadal and Longer Climate Variability

The QuikSCAT data has provided a valuable data set for examining ocean vector wind variability at some scales, but a longer data record is required to understand variability on seasonal, interannual and decadal time scales and to provide additional statistics for characterizing sub-annual variability. QuikSCAT also provides the highest quality and most consistent data set for driving ocean models (although care must be taken to account for the interaction between winds and mesoscale features), but continuation of the highly accurate QuikSCAT data record is required to support ongoing ocean modeling studies. The ISRO OSCAT scatterometer may help bridge the gap when coupled with the continued

QuikSCAT calibration mission. However, the main priority of the ISRO scatterometers is for use in weather prediction, rather than the continuation of a consistent long-term and high-quality data record. For science applications, a mission designed with long-term stability and cross-calibrated with the OVW data record (even if vicariously through QuikSCAT and cross-calibrated OSCAT) is required. The mission should be launched as soon as possible to minimize the effects of data gaps on the OVW record.

2.2 Diurnal and Sub-Diurnal Winds and Constellation Cross-Calibration

An additional requirement for the characterization of long-term changes is the ability to resolve diurnal wind variations. These variations can drive the dynamics of the mixed layer and can be significant along the coasts, impacting the siting of ocean wind turbines, for instance. Sub-diurnal wind variability also confounds the comparison between different scatterometer data records. The temporal sampling that can be achieved by a single scatterometer is insufficient to provide this kind of sampling. Therefore, we recommendation that any future scatterometer mission be coordinated carefully with the existing scatterometer constellation to optimize temporal coverage. Non-sun synchronous orbits, such as the one for the International Space Station (ISS), can help resolve diurnal and semi-diurnal variability and provide coincident data for all members of the scatterometer constellation. This is generally difficult for sun-synchronous orbits, even when multiple satellites are involved.

2.3 High Resolution Winds

A large impact on advancing ocean vector wind science to the next generation would be achieved by improving the spatial resolution of the measurements beyond that 25 km resolution of QuikSCAT (with 12.5 km resolution, but degraded quality, with special processing of the QuikSCAT data). The desired resolution is 5 km or better, but even a resolution of 10 km would improve the understanding of the importance of small-scale features in the wind field, both for scientific applications and for weather forecasting. High-resolution winds will advance the understanding of the coupling between SST and winds by providing data that would be on the same scales as SST fronts, filaments, and other mesoscale features. High-resolution would also enable improved mapping of wind fields in the coastal regions, which are of great societal importance, as most shipping and fisheries occur in a narrow coastal band which is not accessible to current scatterometers. High-resolution winds in the coastal regions would also allow scientific investigation of the impact of persistent wind features such as wind jets, orographic winds, island shadowing, vortex streets, etc., on the ocean circulation and productivity. In addition, high resolution winds can provide significant additional understanding of the dynamics governing mesoscale convective systems, tropical cyclones, and frontal systems, even in the presence of data gaps due to rain (as long as these are properly flagged).

2.4 Driving Science Questions

The following list of questions, reflecting the foregoing science themes, are representative of cutting-edge questions that will drive future scatterometer science missions (we associate questions with a detailed discussions in the following section):

Atmospheric and ocean variability on all time scales

- How do Ocean Vector Winds change on decadal and longer time scales? (Section 3.1)
- What are the modulations of inter-annual variability, including their influence on regional sea level? (Section 3.1)
  - Are these changes related to natural variability or anthropogenic effects?
  - How well do Numerical Weather Prediction (NWP) products and climate models represent the changes? (Section 3.3)
- What are the trends and variability in extreme events (hurricanes, tropical/extratropical storms) and their geographical distribution? (Section 3.13)
- How will a sustained data record improve the fidelity of numerical weather prediction and ocean circulation models? (Section 3.3)

Ocean Atmospheric Coupling

Mesoscale Coupling

- What is the influence of SST on surface winds and associated feedbacks onto the ocean? (Sections 3.6, 3.5)
- What is the influence of SST on tropospheric winds, clouds and precipitation? (Section 3.10)

- What is the effect of diurnal ocean-atmospheric coupling on lower frequencies of variability? (Section 3.2)

Submesoscale Coupling

- What is the ocean-atmospheric coupling at ocean submesoscale and near coasts? (Section 3.5)
- What is the two-way coupling between high-resolution ocean SST/SSH features (eddies, filaments, fronts) and wind/stress? (Sections 3.6 and 3.7).

Latent and Sensible Heat Fluxes

- What impact does wind, and its modulation by SST fronts, play in governing latent and sensible heat fluxes? (Section 3.9)

Coastal Winds

- What are the effects of coastal orography and SST on near shore winds (wind jets, shadows. . .)? (Section 3.5)
- What are the effects of land modulated wind features on coastal circulation and productivity? (diurnal and/or persistent winds) (Section 3.5 and 3.8)
- What is the coupling between SST and winds in the coastal upwelling regions? (Section 3.5 and 3.6)
- What is the effect of coastal surface ocean currents on the wind stress? (Section 3.5 and 3.6)
- How can scatterometer winds improve forecasts for coastal winds, waves, and sea surface temperature? (Section 3.3)

Convection/Precipitation

- What governs the dynamics of tropical mesoscale convection systems? (Section 3.10)
- What are the surface divergences associated with SST and clouds and their effects on precipitation? (Sections 3.10, 3.11, 3.12)
- Characterize and understand the dynamics of mesoscale convective systems in order to evaluate their role and contributions to the energy and water cycle, as well as represent them in numerical weather and climate models. (Section 3.10)

  - Characterize the organization, structure, and surface flux properties within mesoscale systems.
  - Quantify the relative contributions of low-level, moisture convergences and local surface fluxes on the moisture budget within mesoscale convective systems.
  - Provide observations needed to develop and improve convective parameterizations in course-resolution (~100 km grid) global climate models to account for mesoscale processes.
  - Provide observations needed for initializing and verifying mesoscale systems in numerical forecast models that are only beginning to reach sufficient grid resolution to represent and forecast them. (The feature resolution in numerical models is typically about a factor of 5 coarser than the grid spacing.)

Tropical Cyclones

- How will high resolution data help us understand inner core processes of tropical cyclones? (Section 3.13)
- How strongly do surface winds influence changes in hurricane intensity? Are changes in surface winds related to changes in hurricane intensity? (Section 3.13)
- What is morphology of submesoscale surface winds during cyclone genesis? (Sections 3.13 and 3.11)
- How do chlorophyll and primary productivity respond to hurricanes? (Section 3.8)

Ocean Productivity and Ocean Vector Winds

- How do winds, SST fronts, mesoscale and submesoscale ocean features, modulate nutrient availability and temperature via vertical mixing and Ekman pumping? (Sections 3.7 and 3.8)
- How does inclusion of ocean winds, SST, and chlorophyll-a improve satellite-derived estimates of nutrients, pCO2, and air-sea CO2 fluxes? (Section 3.8)

Three

Science Justification

3.1 The Ocean Vector Wind Climate Data Record

Ocean vector wind (OVW) is a key variable for ocean-atmosphere interaction, climate variability and change. Winds interact with atmospheric convection on all timescales. Ocean vector wind is the major driving force for upper ocean circulation, and the interaction of surface wind and SST is a major source of interannual variability in the tropics as illustrated by El Nino/Southern Oscillation (ENSO), as well as decadal and multi-decadal climate variability such as Pacific Decadal Oscillation (PDO) and Atlantic Multi-decadal Oscillation (AMO) (e.g., Mantua et al. 1997; Delworth and Mann 2000). Climate change makes up an increasingly large part of observed climate anomalies. While the rise of global mean air temperature for the recent decades is largely due to anthropogenic increase of greenhouse gases in the atmosphere, detecting and interpreting regional climate change represent a major scientific challenge (Vecchi et al., 2008; Deser et al., 2010). Records for any single climate variable suffer errors that introduce uncertainties in characterizing climate change. It is important to set up an observing system for a set of ocean-atmospheric variables with the kind of consistency that permits the detection of regional patterns of climate change and examination of physical relationship among these variables. Ocean vector wind is an essential variable for ocean-atmosphere interaction and a high priority in the observing system for climate change. Long, consistent observations of ocean vector wind are crucial in detecting regional patterns of climate change in synergy with other observational records including SST, marine cloud, and the thermocline depth (Tokinaga et al. 2012; Figure 3.1).

The annual/monthly mean trend in ocean vector wind is projected to change on the order of 1-2 m/s over the next century. Robust changes projected by climate models include the slow down of the Indo-Pacific Walker circulation (Vecchi and Soden, 2007), accelerated southeast trade winds (Xie et al., 2010), and the intensification and poleward shift of the westerlies in the Southern Ocean (Gillett and Thompson, 2003; Polvani et al., 2011). Some of these changes have begun to be detected from observations but observation errors and natural variability introduce large uncertainties in detecting long-term trends.

To date, our knowledge of the structure and mechanism of decadal and longer variability and changes has been limited by the lack of continuous and consistent time series of global OVW measurements on multi-decadal time scales. Scatterometry is a promising way to detect long-term changes in extreme wind events and atmospheric storms, phenomena of important socio-economic impact.

There exist a few examples of applying scatterometer data to study decadal changes. For example, Lee (2004) and Lee and McPhaden (2008) used wind observations from scatterometer along with altimeter-derived sea level to study decadal changes of ocean circulation and the relation to wind forcing. Lee and McPhaden (2008) found that linear trends of large-scale wind stress (and its curl) in the early to late 1990s (from ERS scatterometers) and in the early to mid 2000s (from QuikSCAT) are opposite in signs in much of the Indo-Pacific domain, reflecting the large decadal signal that encompasses these time intervals. They found evidence of tropical-extratropical and inter-basin teleconnections associated with Indo-Pacific decadal variability. In particular, the decadal oscillation of the Walker Circulation as illustrated by observed zonal wind changes in the tropical Pacific and Indian Oceans linked the decadal variability of meridional property transports in the Pacific and Indian Oceans (Figure 3.2). These observations are insufficient to characterize decadal climate variability in general and far too limited to evaluate the representation of decadal variability simulated by climate models.

Sustained measurements of OVW are indispensible (1) to enhance our understanding of decadal climate variability and its predictability/prediction, to discern the relative contribution of natural climate variability versus anthropogenic climate change, and to project the effects of climate change. Climate consistency is an important metric in designing satellite wind-measuring missions.

3.2 Sub-Daily Wind Variability

Diurnal Coupling in the Tropics

Many coupled modeling studies have shown that diurnal ocean-atmosphere coupling in the tropics has significant rectification both on the background state and on the variability. The rectification effects are associated with changes in both the ocean and atmosphere, including SST and mixed-layer depth, ocean surface wind and ocean current, and convection in the atmosphere. Effects of diurnal coupling on the background state include those on the mean state and that on climatological seasonal cycle while those on the variability include the impacts on the Madden-Julian Oscillations (MJO) and El Nino-Southern Oscillation (ENSO).

Existing coupled climate models are typically characterized by a bias in the representation of the state of the tropical Pacific Ocean and atmosphere such as the common cold bias in the tropical Pacific. Coupled model studies (e.g., Danabasoglu et al. (2006); Bernie et al. (2008); Ham et al. (2010)) showed that the inclusion of diurnal ocean-atmosphere coupling significantly reduced the tropical bias (e.g., Figure 3.3). Bernie et al. (2008) showed that the inclusion of diurnal coupling also has affected the seasonal cycle of the coupled model (Figure 3.4). Coupled models often over-estimate the magnitude of ENSO. The inclusion of diurnal coupling is found to reduce the magnitude of ENSO significantly, i.e., closer to the observed magnitude (e.g., Danabasoglu et al. (2006); Ham et al. (2010)) (Figure 3.5). Bernie et al. (2008) and Kinghaman et al. (2011) found that the introduction of diurnal coupling to the coupled models affected MJO simulation; the magnitude of MJO with diurnal coupling became closer to the observation. Sub-daily measurements of OVW are required to validate the structure of diurnal coupling prescribed or simulated in coupled models (i.e., in terms of the spatial distribution and temporal phasing of OVW, SST, and heat flux associated with diurnal variability).

Sub-daily wind and ocean mixing

Ocean surface wind generates inertial oscillations in the ocean. The latter provide a major mechanism of vertical mixing, which redistribute heat and other properties (e.g., nutrients and carbon) in the water column. Therefore, wind-generated inertial oscillations are important to climate variability and biogeochemistry. At mid- to high-latitude regions, the inertial periods are less than one day. Lee and Liu (2005) and Lee et al. (2008) contrasted the responses of an ocean model to twice-daily and daily wind forcing. The former study was based on NCEP/NCAR reanalysis wind while the latter study was based on the 9 months of QuikSCAT-SeaWinds scatterometer tandem mission data in 2003. Both studies showed that the simulation with daily wind is associated with a warm bias in mid-latitude SSST especially during summertime (Figure 3.6). The experiment with twice-daily wind alleviated this problem. This is because the period of inertial oscillation at mid-latitude is about 12 hours. The twice-daily wind is able to generate more intense inertial oscillation and stronger vertical mixing, which helps minimize the warm SST bias by increasing the mixing with colder subsurface waters.

Existing scatterometer measurements are very limited in monitoring sub-daily OVW. Future scatterometer measurements that capture sub-daily OVW variability would significantly enhance our capability to simulate ocean and atmosphere state both in terms of the mean and variability.

3.3 The Impacts of Scatterometry on Numerical Weather Prediction Models

Scatterometer winds are assimilated into all of the major global numerical weather prediction (NWP) models in use today worldwide. The U.S. National Centers for Environmental Prediction (NCEP) and the European Centre for Medium-range Weather Forecasts (ECMWF) led the way by initiating assimilation of QuikSCAT winds beginning, respectively, on 13 January 2002 and 22 January 2002. Both weather forecast centers found a significant impact of QuikSCAT winds on the skill of their forecasts. However, one has to look closely to see evidence of this impact. An example metric that shows an impact is the global percentage of model winds that differed in direction by less than 20° from QuikSCAT observed winds when collocated in space and time. From the time series of this metric shown in Figure 3.7 (Chelton et al., 2006), it is evident that there were abrupt improvements by about 5% immediately after initiation of QuikSCAT assimilation in each of the models. Other metrics show similarly subtle improvements.

It is easy to find evidence that the NWP models grossly underutilize the information content of scatterometer wind observations. The intensity of any major storm over the ocean is generally underestimated and the storms are often mislocated in space and time in the model forecasts. An example is shown in Figure 3.8 for a storm that occurred in the North Pacific on 10 January 2005 (Chelton et al., 2006).

Underutilization of the information content of scatterometer wind observations is also evident in the surface wind fields of NWP models outside of major storms. This is quantified in Figure 3.9 (Chelton et al., 2006) from wavenumber spectra computed from the NCEP and ECMWF surface winds collocated in space and time to the QuikSCAT measurements. While the spectral rolloff with increasing wavenumber (decreasing wavelength) is approximately k^{-2} for the QuikSCAT observed winds, the spectral rolloff is steeper than k^{-4} and is almost imperceptibly different from each other for the NCEP and ECMWF winds. Both NWP models underestimate the spatial variance of the surface wind field at all wavelength scales smaller than about 1000 km. The underestimation is a full order of magnitude at a wavelength of 350 km and more then two orders of magnitude at wavelengths shorter than about 125 km. The grid resolutions of the NCEP and ECMWF models during the 2004 time period for which the spectra in Figure 3.7 were computed were about 50 km and 40 km, respectively. The underestimation of variance out to wavelength scales of 1000 km therefore cannot be attributed to coarseness of the grid spacing in the models.

Some of the underestimation of small-scale variability in the surface wind fields of NWP models is attributable to underestimation of the ubiquitous influence of sea-surface temperature (SST) on surface winds summarized previously. The observed surface wind response to SST is clearly evident in the surface wind fields of NWP models (see the maps in Figures 3.10b and c). On scales of 100-1000 km, the model winds are higher over warmer water and lower over cooler water. The scales of this surface wind response are critically dependent on the resolution of the SST fields that are used as the surface boundary condition in the model. This is readily apparent from comparison of the maps in Figures 3.10b and c. The Reynolds SST boundary condition used in the NCEP model has much lower resolution than the Real-Time Global (RTG) SST boundary condition used in the ECMWF model. As a consequence, there is much less small-scale structure in the surface wind fields of the NCEP model compared with the ECMWF model.

But even with a perfect SST boundary condition, the NWP models would underestimate the surface wind response to SST by about a factor of two. This is evident from the binned scatter plots in Figures 3.10b and c that show the wind speed response to a given SST anomaly. The coupling coefficients (i.e., the slopes of the lines through the binned scatter plots) are only about half as large as the values inferred from the QuikSCAT observations in Figure 3.10a.

The observed coupling between surface wind speed and SST is also clearly evident in coupled climate models. Coupled models with a low-resolution ocean component do a poor job of representing this air-sea interaction (Figure 3.10d). When the resolution of the ocean component is increased, the SST influence on surface winds becomes much more apparent (Fig. 4e). As in the case of NWP models, however, this coupling is underestimated by roughly a factor of two (see the binned scatter plots in Figures 3.10d and e).

The general underestimation of surface wind response to SST in NWP and coupled climate models is likely attributable to inadequacies of the parameterization of vertical mixing in the models. This hypothesis has been confirmed from a detailed comparison between QuikSCAT winds and the surface winds in the ECMWF model and simulations with the Weather Research and Forecasting (WRF) mesoscale atmospheric model. The use of a vertical mixing parameterization in the WRF model similar to that used in the ECMWF model results in a WRF surface wind response to SST that is almost identical to that found in the ECMWF model, i.e., about a factor of two too small. However, using an enhanced mixing parameterization that has stronger sensitivity to stability in the boundary layer increases the surface wind response to SST to match almost perfectly the response inferred from QuikSCAT observations.

The under-representation of the SST influence on surface winds in most atmospheric models has two important implications. Firstly, since the surface wind response to SST is underestimated, any tropospheric response to SST will also be underestimated. The influence of this ocean-atmosphere interaction on the general circulation of the atmosphere may therefore be considerably misrepresented in present NWP and coupled climate models. Secondly, ocean models forced with the surface winds from NWP models, or coupled to similar atmospheric models, will underestimate any feedback effects on the ocean circulation that the SST-induced small-scale wind forcing may have on the ocean circulation.

The grid resolutions of global NWP models are now approaching those of regional mesoscale models. Currently, the grid spacing for both NCEP and ECMWF is about 20 km. As these grid resolutions continue to get smaller and smaller in an effort to resolve as much of the spectrum of wind variability as possible, scatterometer winds with high spatial resolution will become ever more important for assessing the quality of the NWP winds from diagnostics such as the wavenumber spectra in Figure 3.9 and the maps and binned scatter plots in Figure 3.10. Moreover, high-resolution atmospheric models will be needed to investigate the lower limit of the range of scales over which SST influences the surface winds and the winds aloft. It is imperative that this synergistic use of models, scatterometer wind observations and satellite measurements of SST continue in order to develop a clear understanding of the importance of ocean-atmosphere coupling on scales smaller than the ~100 km scales that are presently resolvable, especially at the submesoscale of less than ~10 km at which it is believed that much of the mixing in the ocean occurs.

3.4 Scatterometer Constellation Cross-Calibration

Ocean vector wind climatologies are important for assessing climate change and forcing ocean circulation models. Due to thermal forcing or moving fronts, the wind over the ocean varies, sometimes systematically over one day, and sun-synchronous satellites will produce climatologies that are snapshots of the winds roughly 12 hours apart (ascending and descending passes).

Although one might think that these temporal scales are more appropriate for weather than climate, the fact that scatterometer systems are typically sun-synchronous introduces systematic biases on the climatological signal. In addition, a symmetric variability in winds will not produce a symmetric variability in wind stress, due to the non-linear relation between the two quantities, and will result in an increase of the mean stress. Figure 3.11 shows how climatologies with significant differences can be obtained when temporal sampling is limited. Similar results were obtained by Lee et al. (2009) by comparing data collected by

SeaWinds on QuikSCAT and ADEOS-II.

Unbiased climatologies can be obtained by increasing the number of scatterometers in the constellation and placing them optimally so that sub-diurnal signal are resolved. If this is not possible, one can estimate the systematic variations by fitting the climatologies collected at different times of day with diurnal and sub-diurnal harmonics (Gille et al., 2003, 2005). These harmonics can be removed to obtain an unbiased climate record. The first estimate of these diurnal variations was undertaken by Gille et al. (2003, 2005), using the QuikSCAT and SeaWinds missions. However, the accuracy of these results was limited by the short duration of this constellation, due to the failure of ADEOS-II. This early demise did not allow for the examination of the seasonal or yearly variations of the diurnal cycle.

Attempts have been made to estimate the diurnal cycle using QuikSCAT and ASCAT data. Although promising, these results are limited by the complications of cross-calibrating two scatterometers which use different frequencies and model functions and acquire data at different times of day. The lack of temporally coincident data, especially in the tropics where diurnal variations are stronger, complicates the cross-calibration of these two instruments. An ideal cross-calibrator would consist of a satellite on a non-sun-synchronous orbit, which could obtain simultaneous measurements every orbit from each member of the constellation. Another advantage of a scatterometer on a non-sun-synchronous orbit is that it will be able to independently resolve diurnal and subdiurnal signals, as explained below.

3.5 Coastal Winds

Ocean-atmospheric properties (SST, marine nutrients and biomass, thermocline depth, cloud, boundary layer height, pollutants, etc) display rapid transitions in coastal zones. From the open ocean toward the shore, ocean vector wind changes both direction and speed. Typically wind speed weakens toward the shore because of increased friction on land but coastal mountains can cause intense wind jets offshore as off the coasts of California (Dorman and Winant, 1995), Central America (Chelton et al., 2000), and Hawaii (Yang et al., 2008). Such spatial variations in coastal winds are important for ocean currents, upwelling, marine biological activities, and fisheries (Figure 3.12).

The ability to measure close to the coast and resolve coastal variability is determined by the scatterometer resolution, i.e. the size of a footprint including side lobes. The size and position of side lobes is the key consideration in retrieving winds near land. If there is too much signal from land, it overwhelms the signal from the water. Therefore, observations with too much signal over land are flagged as bad, and not used in wind retrievals. This problem can be greatly reduced by using finer scale footprints or reduced sidelobes.

Advantages of finer resolution (see Figure 3.13) are observations much closer to the coast and the ability to much better resolve the curl and divergence, which are important for ocean forcing and cloud formation. The finest scale winds (Figure 3.13) show a vorticity gradient near the coast, indicating that near coastal ocean forcing is should not be extrapolated from the open ocean.

In time, coastal winds display rich variations. Forced by land-sea thermal contrast, diurnal variations are strong and increase in amplitude toward the coast. Coastal winds respond strongly to atmospheric synoptic disturbances especially near topography (e.g., Santa Anna winds; Hu and Liu (2003)). On interannual timescales, coastal winds vary speed and direction in response directly to atmospheric circulation change (e.g., off the west coast of North America in association with Aleutian low variability), and indirectly to ocean coastal waves (e.g., off the South American coast during El Nino). Surface air temperature warming in response to increased atmospheric greenhouse gas concentrations is expected to be considerably larger over land than ocean. This change in land-sea contrast is likely to affect coastal winds and their diurnal cycle. Past and current scatterometers have detected broach coastal wind structures but the satellite observations are limited by spatial resolution and to regions 50 km or more offshore, missing the near-coastal zones where stronger variations are expected. Improving spatio-temporal resolution and pushing the observations closer to the coast are a priority for future scatterometer missions.

3.6 Influence of Mesoscale SST Fronts on Surface Winds

Satellite and in situ measurements of surface wind stress and sea surface temperature (SST) show a strong coupling and positive correlation on spatial scales of 100-1000 km (see reviews by Small et al. 2008 and Chelton and Xie 2010). Mesoscale SST variability drives perturbations in surface heat fluxes, which influences the surface winds through intermediary responses of the marine atmospheric boundary layer (MABL) pressure and turbulence fields to these SST-induced surface heating perturbations.

Maps of 7-year averaged wind speed from the QuikSCAT scatterometer and SST from AMSR-E over four mid-latitude regions (Figure 3.14) show this high correlation between the surface wind speed and SST (O'Neill et al., 2012). The fields in these maps have been spatially high-pass filtered to highlight the strong covariability on these spatial scales.

Much has been learned about the surface wind response to ocean fronts from the QuikSCAT wind observations. Transitions in SST which give rise to these wind perturbations, however, can occur over spatial scales much smaller than the 25 km footprint of individual QuikSCAT observations. An example is shown in Figure 3.15 from aircraft wind observations at 30-m height over the Gulf Stream off the Outer Banks of North Carolina during the SHOWEX field campaign conducted Nov. 20, 1999 (Mahrt et al., 2004). The influence of the sharp SST change across the Gulf Stream, shown in the top panel, causes a large acceleration of the surface winds over a distance of ~10 km. A map of the QuikSCAT wind vectors and AVHRR SST for Nov. 20, 1999 (Figure 3.16) shows the location of the in situ observations within the blue circle. Two versions of the QuikSCAT wind vectors are shown: one with 25 km resolution shown in magenta, and one with 12.5 km resolution shown in black. Both versions miss important details of the wind transitions across the sharp Gulf Stream SST front shown by the in situ observations in Figure 3.15.

While in situ observations have been of enormous benefit to characterize interactions between SST and surface winds, in situ observations are generally limited to localized case studies over relatively short timescales ($\leq$1 week). Surface wind measurements with high spatial resolution over a sustained period would yield enormously beneficial information on the statistics of the surface and boundary layer response to spatially varying SST over many regions of the World Ocean. This information will be invaluable for improving weather forecast and ocean circulation models, since interactions on these small spatial scales are not resolved in the models and are potentially very important for affecting weather and ocean circulation. This information will be crucial to improving our understanding of the feedback onto the ocean of the SST-induced surface wind perturbations.

An example of the sensitivity of the wind-driven circulation of the ocean to these small-scale wind perturbations is shown in Figure 3.17. The top panel shows a first-order estimate of the vertically-integrated ocean transport caused by the surface wind stress (called the Sverdrup transport) for a 5-year period 2002-2007. The bottom panel shows the Sverdrup transport once the small-scale wind perturbations have been spatially-smoothed, thus effectively removing the direct influence of mesoscale SST features on the surface winds discussed above. The difference in the ocean transport is quite remarkable, where mesoscale wind variability leads to a narrower and more intense Gulf Stream and secondary recirculation gyres throughout the North Atlantic.

3.7 Mesoscale Eddy Influence on the Surface Stress and Oceanic Chlorophyll

The surface stress is altered over the cores of oceanic mesoscale eddies by two distinct mechanisms. The first of these is through the same air-sea interaction process discussed previously in which sea-surface temperature (SST) influences the overlying wind field. The other is through an eddy-induced surface stress that arises from the difference between the surface velocity of the rotating eddies and the surface vector wind field. As summarized below, both of these processes result in a curl of the surface stress, which in turn generates Ekman upwelling and downwelling that influences the biology within the eddy cores.

Collocation of satellite-based estimates of SST to the interiors of mesoscale eddies inferred from their sea-surface height (SSH) signatures reveals that the dominant influence of eddies on SST is a horizontal stirring of the ambient SST field from advection by the rotational velocity within the eddy interiors. This results in dipole SST anomalies of opposing signs in the eddy interiors that depend on the direction of the ambient SST gradient and on whether the eddy rotates clockwise (CW) or counterclockwise (CCW) (Figures 3.18a,b and 3.19). From collocation of scatterometer measurements of surface winds to the eddy interiors, it becomes evident that this eddy-induced SST variability influences the wind field over the eddy interiors by the same mechanism that has been studied extensively in the past in the context of frontal air-sea interaction. As shown in Figures 3.18c,d, the geographical distribution of surface wind speed over the eddy interiors is virtually identical to the dipole structures of SST within the eddies. A quantitative analysis concludes that the wind speed distribution within these dipoles is linearly related to SST with a coupling coefficient that is consistent with that estimated previously in frontal regions. Wind speed is higher and lower, respectively, over the warmer and colder portions of the eddy-induced SST dipole.

The horizontal variation of the SST-induced surface winds over the interiors of mesoscale eddies results in a wind stress curl that is proportional to the crosswind SST gradient. The Ekman pumping velocity associated with positive and negative wind stress curl generates, respectively, upwelling and downwelling within the eddy interior. Simulation of this two-way coupling in a numerical model of an idealized eastern boundary current system shows that these feedback effects significantly influence the mesoscale eddy field. Because of ageostrophic effects, the SST gradients associated with cyclonic eddies are stronger than those of anticyclonic eddies. The feedback effects on the ocean from SST-induced perturbations of the wind stress curl field therefore preferentially disrupt the coherent evolution of cyclonic eddies, resulting in a greater abundance of anticyclonic eddies.

In addition to the feedback effects of the above ocean-atmosphere interaction from SST influence on surface winds, the eddies can generate self-induced Ekman pumping from the surface stress that arises from the difference between the surface vector wind and the surface water velocity. Since winds usually have scales larger than the order 100-km diameters of mesoscale eddies, the vorticity (curl) of the relative wind (surface vector wind minus surface water velocity) over eddies is determined primarily by the surface water velocity within the cores of the eddies. This relative wind is the wind that is measured by a scatterometer. The vorticity of a rotating eddy generates a vorticity of opposite sign in the relative wind. Anticyclonic and cyclonic eddies thus generate positive and negative wind stress curl and therefore Ekman upwelling and downwelling, respectively.

A detailed analysis of the collocated satellite measurements of SST, geostrophic velocity computed from SSH, and wind stress curl to the eddy interiors concludes that the relative importance of the above two mechanisms for Ekman pumping over the cores of mesoscale eddies varies geographically. In regions of strong SST gradients (e.g., near SST frontal regions), air-sea interaction over the SST dipoles is important. In the open ocean away from strong SST fronts, however, surface current-induced Ekman pumping is generally of greater importance.

As shown in Figures 3.20 and 3.21, composite averages of the wind stress curl and associated Ekman pumping computed from SSH based on the surface geostrophic velocity of open-ocean eddies agree well with composite averages of the wind stress curl computed from QuikSCAT observations of surface wind stress. The detailed structures of the surface current-induced Ekman pumping field over mesoscale eddies vary geographically, depending on the steadiness of the wind direction. Because of the nonlinear relationship between wind and wind stress, the instantaneous wind stress curl associated with an axially symmetric vorticity of the relative wind is elongated in the direction of the wind. This instantaneous elongation becomes blurred in time averages if the wind direction is variable. The effects of this blurring are apparent from Figures 3.20 and 3.21. A zonally elongated structure is evident for the northeast tradewinds region of relatively steady wind direction (Figure 3.20). The more circular structure in Figure 3.21 for the South Indian Ocean is because the wind direction is highly variable in this region.

The importance of surface current-induced Ekman pumping is evident in specific regions where anticyclonic eddies trap high concentrations of phytoplankton at their time of formation. This is most clearly seen in composite averages of the chlorophyll in anticyclonic eddies that form in the Leeuwin Current along the west coast of Australia (left panel of Figure 3.22). Surface current-induced Ekman upwelling in these anticyclones can sustain the trapped phytoplankton as the eddies propagate considerable distances away from the Australian coast, sometimes for several years. In contrast, the Ekman downwelling over the cores of cyclonic eddies in this region results in a deficit of chlorophyll. This influence of Ekman pumping is most evident in the wintertime, probably because the mixed layer depth is sufficiently deep to "kiss" the nutricline, thus allowing the injection of nutrients into the eddy interior where they can be utilized by the phytoplankton trapped in the eddy core.

The understanding of the above two eddy-induced mechanisms for Ekman upwelling over the interiors of eddies is limited to the relatively large radius scales of order 100 km that are resolvable in SSH fields constructed from multi-mission altimeter data. It can be anticipated, however, that these effects are also important on smaller scales down to the submesoscale of less than 10 km. It is known observationally that the SST gradients and surface velocities of submesoscale features are both very intense. Since the surface velocity of submesoscale variability varies over small scales, the wind stress curl and associated Ekman pumping generated by surface current-induced stress is likely to be very strong over submesoscale features. The importance of Ekman pumping associated with air-sea interaction on submesoscales is less clear since it is not yet known how winds respond to SST on small scales. High-resolution scatterometer winds are needed to understand the importance of both mechanisms for small-scale Ekman pumping to submesoscale ocean dynamics and biology, as well as to further improve the understanding of this physical-biological interaction on larger mesoscales.

3.8 Ocean Productivity, Sea Surface Temperature, and Ocean Vector Winds

How do winds modulate nutrient availability and temperature via vertical mixing and Ekman pumping?

Changes in the physical and biological state of the ocean are closely associated with ocean surface wind on various spatial and temporal time scales. Such a relationship has been illustrated in numerous studies that utilize satellite-derived measurements of sea surface temperature (SST), ocean color (chlorophyll-a or chl-a), and ocean vector winds (e.g., Stramma et al., 1986; Babin et al., 2004; Gierach and Subrahmanyam, 2007, 2008; Barton et al., 1993; Chelton et al., 2000; Rodriguez-Rubio and Stuardo, 2002; McClain et al., 2002; Xie et al., 2005b; Liang et al., 2009). Fluctuations in the wind field perturb the ocean state impacting vertical processes (e.g., vertical mixing and upwelling) that affect the redistribution of ocean properties within the water column (Figures 3.23 and 3.12). For example, hurricanes and gap jets are associated with accelerated winds that induce vertical mixing and upwelling, which bring cooler, nutrient-rich subsurface waters to the ocean surface. Based upon the (generally) inverse correlation between temperature and nutrient concentrations, SST cooling is usually considered a proxy for nutrient injection into the surface layer. Nutrient influx coupled with adequate sunlight stimulates phytoplankton growth and can produce phytoplankton blooms several days after an event. Within satellite imagery, these responses are observed as decreased SST (or SST cooling) and increased chl-a concentrations relative to adjacent waters (Figures 3.23 and 3.12). High-resolution SST and ocean color observations are available to characterize the biophysical response to synoptic events; however, the same is not true for winds (i.e., the driving mechanism for the biophysical responses observed) because of the relatively low spatial resolution of satellite wind measurements. To better understand and characterize wind-induced vertical mixing and Ekman pumping in space and time, higher-resolution satellite winds are necessary.

How does inclusion of ocean winds, SST, and chlorophyll-a improve satellite-derived estimates of nutrients, pCO2, and air-sea CO2 fluxes?

Simultaneous observations of SST, ocean color, and winds have implications to the carbon cycle. Specifically, simultaneous high-resolution observations are required to effectively capture the time-space variability in ocean characteristics that regulate carbon (e.g., nutrients and ocean pCO2) (Figures 3.24–3.25). Nutrient concentrations are not a direct measurement made from satellite, but can be globally estimated through application of satellite imagery to algorithms based upon relationships between temperature (possibly chl-a) and nutrients (Figure 3.24) Kamykowski et al., 2002; Goes et al., 1999, 2004 illustrated that co-registered, simultaneous SST and chl-a imagery improved satellite estimates of nitrate at basin to global scales. Additionally, several studies have illustrated the use of SST or simultaneous SST and ocean color to estimate surface seawater pCO2 that were then used in combination with ocean winds (from models and satellite) to estimate air-sea CO2 fluxes (Figure 3.25) Stephens et al., 1995; Nelson et al., 2001; Olsen et al., 2004; Wanninkhof et al., 2007. These studies likely underestimated air-sea CO2 fluxes given utilization of coarser-resolution wind fields. Higher-resolution satellite winds would improve global, regional, and coastal estimates of air-sea CO2 fluxes.

3.9 Latent and Sensible Heat Fluxes

The interplay between over-ocean fluxes and over-ice fluxes is a very important part of the high latitude climate (Gille et al., 2010). The high latitude fluxes also contribute to deep water formation (Moore and Renfrew, 2005). Recent advances in satellite retrieval techniques has enabled improved input data for ocean surface fluxes of momentum, moisture, latent heat, and sensible heat to be collected at a relatively good combination of temporal and spatial sampling (Bourassa et al., 2010).

The observational capability of surface turbulent fluxes would be enhanced by the combination of an AMSR3 and scatterometer on the same platform. Satellite-retrieved data have the potential to significantly reduce the biases and sampling errors associated with these fluxes and budgets for large and small areas, enhancing NASA's energy and water cycle goals. A bulk-aerodynamic approach is used to calculate moisture, latent heat, and sensible heat fluxes. The AMSR and/or SSMIS data provide SST, near surface humidity and near surface air temperature (Jackson et al. 2009; Roberts et al. 2009). The scatterometer can provide the wind speed required for the bulk formula.

3.10 Atmospheric convective system

Atmospheric convection interacts strongly with circulation. Latent heating in convection drives circulation while moisture transported by circulation fuels convection. The Madden-Julian Oscillation (MJO), of a 30-60 days timescale and planetary scale in space, results from this interaction. Atmospheric convection is organized in a hierarchy of structures: individual cumulonimbus clouds are of 10 km in scale, and are organized into cloud clusters of 100 km scales (mesoscale convective systems; Zuidema 2003; Houze 2004). These cloud clusters are further aggregated into an envelope of active convection of several thousand km in zonal extent, propagating eastward as part of the MJO (Nakazawa, 1988). Very pronounced in observations and of global influence, MJO remains a major challenge for atmospheric model simulation (Lin et al., 2006) because of the difficulty representing the hierarchy of convective structures and their interactions. Attempts are being made to explicitly resolve mesoscale convective systems with global atmospheric models of horizontal resolution of 10 km and finer, run on the world's fastest computers. The results show great promise that such cloud-resolving models can improve the simulation of mesoscale convective systems and hence MJO (Miura et al., 2007). Direct observations of mesoscale convective systems are limited to a few field campaigns and there is an urgent need for extensive observations to study the structures of mesoscale convective systems and validate the emerging global cloud-resolving models.

At 25 km resolution, QuikSCAT can marginally resolve wind structures of large cloud clusters (Figure 3.28). With enhanced resolution (10 km or better), scatterometry will reveal key dynamical features of mesoscale convective systems, such as wind gusts associated with cold pools, features considered essential to sustain these systems. For a single scatterometer mission, it is desirable to have a co-orbiting microwave radiometer to put wind variations in the context of mesoscale convective systems. Simultaneous measurements by microwave radiometer and scatterometer facilitate studies of convection-SST interaction on the mesoscale and can test the hypothesis that warm mesoscale SST patches are instrumental in the onset of mesoscale convective systems (Li and Carbone, 2012).

3.11 High Resolution and Rain Flagging

The main weaknesses of scatterometers are rain contamination for some rain conditions (far more so for Ku-band than C-band), a lack of data near land (15 km for QuikSCAT; 30 km for ASCAT; >30 km for OSCAT), and temporal sampling (Bourassa et al., 2010). Multiple scatterometers greatly improve the temporal sampling (Liu et al. 2008; D. Chelton, personal communication, 2011). Finer resolution will improve the quality of rain flags and provide more data in near coastal regions. Rain flags are particularly important for the wind derivative fields, which are inherently noisy when determined from scatterometer observations (Bourassa and McBeth-Ford, 2010). The finer spatial resolution greatly reduces the noise for the same spatial averaging scale, allowing more accurate calculations closer to the coast. The rain flags will also be of interest when linking surface convergence to AMSR3 estimates of precipitation. The combination of precipitation estimates and surface vorticity are also likely to be advantageous for examining the very early stages of cyclogenesis (Gierach et al. 2007; Bourassa and McBeth-Ford 2010).

The accuracy of rain flags is also important for a wide range of ocean forcing. The greatest percentage wind errors often occur in the tropics where the wind speeds are typically low and the rain rate can be large. Rain errors are typically larger in the across swath direction, making the greatest errors in the zonal wind component. In the equatorial oceans, rain can cause huge errors in the wind forcing unless the rain impacts are wind are properly removed or corrected (Owen and Long, 2011). Similarly, large errors can also occur in high wind speed storms with heavy precipitation, as shown for wind speed (Draper and Long, 2004; Bourassa et al., 2010) and vorticity (Bourassa and McBeth-Ford, 2010).

High resolution and rain flags are also useful for examining mid-latitude systems. Such systems can be rain-free in areas with hurricane force winds; however, they do have rain and strong gradients in wind speeds near atmospheric fronts. An model example of the core of such an intense system is shown in Figure 3.29. Away from these features, 15 km resolution is good for most applications; however, finer scale is desirable for calculating curl and divergence. Bourassa and colleagues are in the process of determining if ultra-high resolution QuikSCAT (roughly 2.5 km resolution, but noisy) are sufficient for such derivative fields. It would be very interesting to produce simultaneous wind and rain retrievals (Owen and Long, 2011) in combination with surface convergence, AMSR3 precipitation, and combined AMSR3 and scatterometer estimates of evaporative fluxes.

Numerical model experiments were conducted to address the previously unexplained anomalously high storm surge along the Florida coast of Apalachee Bay during Hurricane Dennis (2005). The 2-3 m surge observed during this storm cannot be obviously explained by the relatively weak local winds over this bay 275 km east of the storm center. Realistic (using HWIND for fine resolution winds in both space and time; 15 km or larger away from the eye wall, and 6 hourly) and idealized numerical experiments demonstrate that a remotely forced continental shelf (topographic Rossby) wave contributed significantly to the sea level rise in the northeastern Gulf of Mexico (Morey et al., 2006). The alongshore winds to the east of the storm center built a high sea level anomaly along the coast which traveled northward to Apalachee Bay as a topographic Rossby wave. The wave was amplified as the storm moved nearly parallel to the shelf and at comparable speed to the wave phase speed. The aircraft data assimilated into H*Wind contributed to the quality of the wind fields near the coast. The differences in surge forecast (Figure 3.30) are quite substantial, with the surge based on finer resolution winds being much more accurate. A constellation of at least three scatterometer in low earth orbits would be required for similar temporal sampling. The fine resolution hurricane winds, with flags for rain contamination, were critical for this kind of study. Combined wind and rain retrievals from a collocated AMSR3 and scatterometer would likely improve the wind fields and the storm surge forecasts.

3.12 Rain Estimation Using Ku and Ka Scatterometry and AMSR

The strong frequency dependence of the rain cross section and the complementary information contained in active and passive measurements, make the combination of a Ku and Ka active radar, together with a multi-frequency radiometer a promising combination for estimating precipitation.

In this section, the main atmospheric (and surface) variables that are responsible for the signals measured by active and passive microwave instruments over precipitation are identified. The explicit relations between the microwave measurements that will be made by AMSR and a Ku/Ka-band scatterometer over a precipitating system, on one hand, and the underlying physical variables, on the other hand, are then derived. The relations show the complementarity of the active and passive observations.

These relations are derived under the simplifying assumption that the radiometer and the radar have coincident beams. In practice, the radiometer beam at the lower radiometer frequencies will be wider than the Ku-band radar beam, which itself will be wider than the Ka-band radar beam. We therefore summarize a novel approach to use the highest-resolution measurement(s) to sharpen the resolution of the coarser-resolution measurements. While this procedure does introduce some additional uncertainty, it will make it possible to perform joint retrievals using all the coincident simultaneous measurements at the highest resolution, thus minimizing the uncertainty in the resulting estimates.

Figure 3.31 illustrates the measurements that would be made by a coincident radiometer and radar with incidence angles near 45o. The radiometer measures the top-of-atmosphere brightness temperature, caused by 1) the surface emission, attenuated by the water in the atmosphere, 2) the up-welling emission from the condensed water in the atmosphere, with the emission from each horizontal layer attenuated by the condensation in the layers above it, and 3) the down-welling emission from the condensed water in the atmosphere, attenuated on its way to the surface, then reflected by the surface and finally attenuated on its way back up to the top of the atmosphere. The radar echo, on the other hand, is proportional to the sum of the backscattering cross-section of the condensed water in the range-resolved volume elements and the cross-section of the surface intersecting the range bin, attenuated by the condensation along the path from and back to the radar. The radar echo can therefore be weak because the surface did not backscatter much, or because the attenuation due to the rain was strong. To sort out the two mutually ambiguous effects, additional independent measurements of the rain are necessary.

Analyses of cloud-resolving model simulations (Bauer, 2001; Coppens et al., 2000) and of TRMM retrieved vertical profiles of precipitating water content (Haddad and Park, 2009, 2010) have confirmed that the first three vertical principal components capture over 75% of the variability of the water content in a precipitating column (the exact portion of the variability depends on whether one can assume to know a priori the rain regime). The first principal component q'_1 is a weighted average of the condensed water contents below the freezing level, while the second and third principal components q'_2 and q'_3 characterize the difference between precipitating liquid and the water content in the solid or mixed phase layers (as illustrated in Figure 3.32, which gives the coefficients of these principal components).

In a simplified atmosphere where the temperature profile is determined by the surface temperature T_s and the constant lapse rate t', the coefficients of the principal components q'_1, q'_2 and q'_3 (expressed as linear combinations of the actual condensed water contents at the different heights in the atmosphere) can be given relative to the melting level T_s/t'.

Neglecting multiple scattering for simplicity, the brightness temperatures Tb depend on the absorption coefficient k_a and on the scattering coefficient k_s of the condensed water, both of which have an approximate power-law dependence on the water content q,

$$\begin{aligned} k_a &= \alpha q^\beta \\ k_s &= a q^b \end{aligned}$$

where the coefficients a, b, α and β do depend on the distribution of the sizes of the hydrometeors that make up q. Figure 3.33 illustrates the individual constituents of $k_a + k_s$ as a function of the individual hydrometeor size. For a given vertical profile $q(h)$ of the water content (varying with height h), the corresponding top-of-the-atmosphere brightness temperature will be approximately

$$\begin{aligned} T_b = & \left[\int_0^\infty k_a(q(h))\, T(h)\, e^{-\int_h^\infty k_a + k_s(q(h'))dh'}\, dh\right] \\ & + T\,\epsilon(w)\, e^{-\int_0^\infty k_a + k_s(q(h))dh} \\ & + \left(\int_0^\infty k_a(q(h))\, T(h)\, e^{-\int_0^h k_a + k_s(q(h'))dh'}\, dh\right) \\ & \times (1-\epsilon(w))\, e^{-\int_0^\infty k_a + k_s(q(h))dh} \end{aligned}$$

representing the upwelling emission from the condensation (the first term, in brackets), the emission from the surface (the second term), and the downward emission from the condensation that is reflected by the surface and attenuated on its way back up to the top of the atmosphere. Since $q(h)$ is a function of q'_1, q'_2 and q'_3 and since $T(h)$ is a function of T_s and t', the equation above makes it clear that the brightness temperatures are functions of q'_1, q'_2, q'_3, w, T_s and t', a total of 6 essentially independent variables. Unfortunately, analyses by different groups (Bauer, 2001) have shown that the information content of the multiple-window-channel radiometer measurements over rain boils down to between 2 and 3 independent observations. Indeed, the main signature of the condensed water is an emission signature at the lower frequencies, and a scattering signature at the higher frequencies, as illustrated in one instance of TMI observations over the Atlantic ITCZ in Figure 3.34.

That is where the radar measurements, which also depend on q'_1, q'_2, q'_3 and w, play a crucial role. Indeed, as figure 5 illustrates, their dependence on the precipitation is quite different from that of the brightness temperatures, and their information content complements that of the passive measurements to allow a far less ambiguous retrieval of the underlying precipitation and wind. Neglecting the multiple scattering, the radar return from range r can be written as

$$\begin{aligned} z &= \sigma^o(w)\, e^{-\int_h^\infty k_a+k_s(q(h))dh} \\ &+ \int\int\int_{\Delta(r)} \sigma_b(q(h_r + r'\cos\theta)) \times \\ &e^{-\int_{h_r+r'\cos\theta}^\infty k_a+k_s(q(h))dh}\, \frac{r'\,dr'\,d\theta\,dh}{\text{volume}(\Delta(r))} \end{aligned}$$

where $\Delta(r)$ represents the tilted cylindrical volume element across the beam around range r, and that integral is therefore over the water contents q within that resolution element. For simplicity, the water contents are assumed to depend only on height, i.e. on the cross-beam coordinate $h_r + r'\cos\theta$ with h_r the height at the center of the volume element. The dependence of the surface back-scattering cross-sections $\sigma^o(w)$ on w is assumed to be known (e.g., from the geophysical model functions at Ku and Ka bands), and the backscattering cross-sections $\sigma_b(q)$ depend not just on the water content but also on the size distribution of the hydrometeors that make up q (see Figure 3.35). The main point here is that all the water contents in this radar equation, as in the case of the radiometer equation above, can be re-written (approximately) as linear combinations of the three vertical principal components q'_1, q'_2, q'_3. Since these principal components are derived empirically from cloud-resolving model simulations, the microphysical parametrization used in each simulation allows one to calculate the radiometric and radiative signatures in the radar and radiometer equations above quite accurately. We thus end up with forward equations that explicitly express the dependence of the 2 radar measurements from each range resolved volume element on the competing backscattering and extinction signatures of the wind-driven surface and the water content principal components, and the dependence of the handful of radiometer measurements on the competing extinction and absorption signatures as well as the 2-parameter simplified temperature profile. Different retrieval approaches can then be considered, including a Bayesian approach to estimate the underlying conditional means of q'_1, q'_2, q'_3, w, T_s and t', (conditioned on the simultaneous measurements) and their joint uncertainties.

Implicit in the derivation of the relations above is the simplifying assumption that the radiometer and the radar have coincident beams. In practice, the radiometer beam at the lower radiometer frequencies will be wider than the Ku-band radar beam, which itself will be wider than the Ka-band radar beam. To address these discrepancies, we developed a Bayesian approach to use the highest-resolution measurement(s) to sharpen the resolution of the coarser-resolution measurements, and thus allow the coarser resolution measurements to be "down-scaled" to the resolution of the Ka band radar measurements, so that joint retrievals at that resolution can be performed. The approach is based on the Bayesian premise that in order to estimate the conditional probability density function $p(t|T, \sigma^o)$ of a fine-resolution version t of a coarse-resolution measurement T, which is conditioned on T and on a related fine-resolution measurement σ^o ("related" meaning with a known conditional mean relation $t_m(\sigma^o)$ that has a known covariance C_m), one has

$$\begin{aligned} p(t|T, \sigma^o) &= p(T|t, \sigma^o)\, p(t|\sigma^o) \qquad \text{(up to an overall constant factor)} \\ &\simeq p(T|t)\ \exp\left[-0.5(t - t_m(\sigma^o))^t C_m^{-1}(t - t_m(\sigma^o))\right] \end{aligned}$$

(because σ^o is superfluous in the first factor on the right, and because we are assuming that we know the ocnditional mean and covariance of $t|\sigma^o$),

$$\approx exp\left(-0.5(T - At)^t C_o^{-1}(T - At)\right)\ \exp\left[-0.5(t - t_m(\sigma^o))^t C_m^{-1}(t - t_m(\sigma^o))\right]$$

where A is the antenna pattern that specifies how the fine-resolution t are convolved to produce the observed coarser-resolution T, up to a pre-specified error covariance C_o (and the second factor on the right is unchanged). Being (approximately) the product of two Gaussians, the result is itself Gaussian, and its mean can be found by "completing the square" in the exponent, or, equivalently, finding the t that maximizes that exponent. It is straightforward to show that that t is given by

$$t\ =\ (1 + C_m A^t C_o{-}1A)^{-1}\left[t_m(\sigma^o) + C_m A^t C_o^{-1} T\right]$$

or, equivalently,

$$t\ =\ t_m(\sigma^o) + (1 + C_m A^t C_o{-}1A)^{-1} C_m A^t C_o{-}1\left[T - At_m(\sigma^o)\right]$$

This equation can be used effectively to find the best (i.e.\ minimum variance, unbiased) estimate of the fine-resolution (Ka-band radar) version t of our coarse-resolution measured brightness temperatures T, assuming we have a mean radar-radiometer relation $t_m(\sigma^o)$. One way to derive the latter is empirically, using simulations from which we can tabulate the forward-calculated simultaneous σ^o and T.

3.13 Tropical Cyclones

While our knowledge of tropical cyclones (TCs) has increased tremendously in the past several decades, the understanding and forecasting of hurricane genesis and rapid intensity changes still remains a significant challenge. Indeed, a major goal of NASA's Hurricane Science Research is improving the knowledge about the critical physical processes and evaluation of their representation in numerical models. Recognizing the high societal value of accurate hurricane forecasts, the NOAA-led, multi-agency 10-year Hurricane Forecast Improvement Project (HFIP) was established in 2007.

Several years into the HFIP project significant progress has been made in several areas. However, even now " ... none of the HFIP dynamical models are ca-pable of providing reliable forecasts of RI [Rapid Intensification] reliably in the first 36 hours." (2011 HFIP annual report). As stated in a recent NRA (ROSES11-HSRP), the current limitations result from " ... poor understanding of the processes involved in intensity change, their representation in numerical models, and a limited ability to obtain detailed measurements of the storm environment and inner-core region ... ".

Previous studies have shown that QuikSCAT data can provide useful information about processes occurring near the periphery of storms in regions of gale-force or lower winds (Knaff et al, 2011). The utility of data closer to the center of the storm is currently compromised by poor resolution, rain contamination, and reduced sensitivity to increased winds at higher speeds. Improved resolution would remove the first obstacle. Co-location with a microwave radiometer such as AMSR can be used to overcome the rain contamination problem. Recent work (Stiles et al., 2012) suggests that all these issues may be surmountable. A neural network approach similar to that used in Stiles et al., 2010 has been em-ployed to produce improved wind fields for all named storms overflown by QuikSCAT from October 1999 to November 2009. The neural network combined several types of data in order to achieve this purpose including QuikSCAT Ku-band backscatter data from multiple polarizations, azimuth angles, and spatial scales, as well as scatterometer-derived brightness temperature estimates (Ahmad et al., 2005). The neural network was trained to map this multidimensional input data to ground truth from NHC H*WINDS wind speeds for 2005 Atlantic hurricanes. The resultant mapping was then used to determine wind speed as a function of backscatter and brightness temperature. An example neural network hurricane wind field is depicted in Figure 3.36. On the website http://tropicalcyclone.jpl.nasa.gov these wind fields can be accessed through a user friendly GUI interface for each year, basin, and storm name (Hristova-Veleva et al., 2008). The neural network wind speeds compare favorably with best track maximum wind speeds from the National Hurricane Center (NHC) and the Joint Typhoon Warning Center (JTWC) as depicted in Figure 3.37. They are also consistent with Step Frequency Microwave Radiometer (SFMR) winds from aircraft overflights of Atlantic storms up to hurricane-force wind speeds (Figure 3.38). High resolution Ku-band scatterometry is a potential avenue for exploring wind processes near the center of tropical cyclones.

3.14 Section 3 Figures

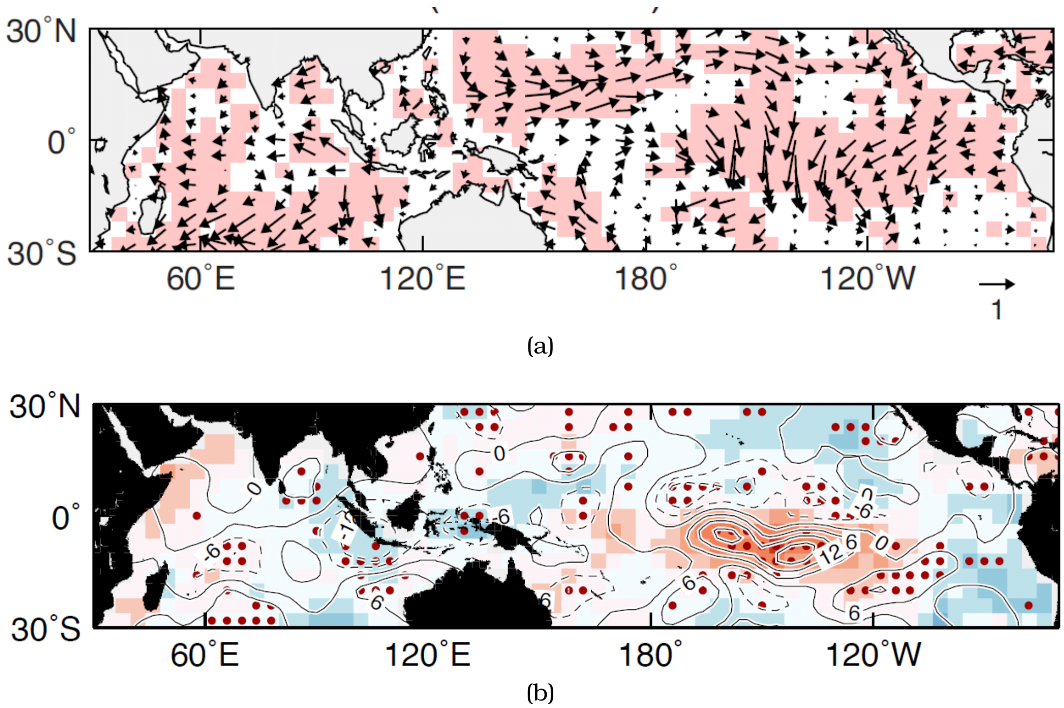

Figure 3.1: Annual mean changes for 1950–2008 based on ship observations: (Upper panel) surface wind (m s^{-1} $(59yr)^{-1}$), and (lower) surface moisture-flux convergence (contours at 6 x 10^{-6} g kg^{-1} s^{-1} $(59yr)^{-1}$Trends exceeding the 90% confidence level are marked with red shade (upper) and circles (lower). The 59-yr changes in marine cloudiness are superimposed (shading in okta $(59yr)^{-1}$). From Tokinaga et al. (2012).

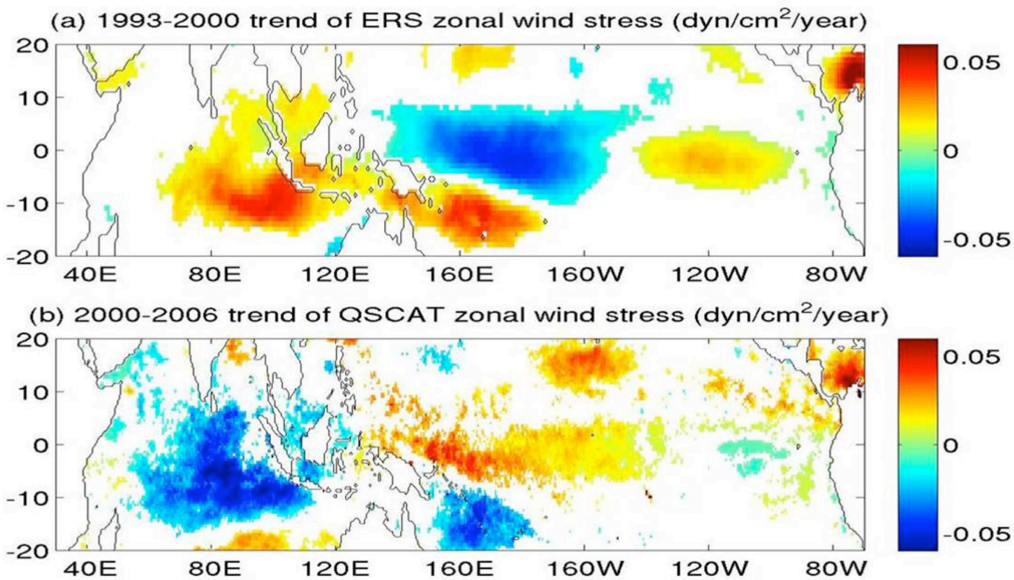

Figure 3.2: Linear trends of zonal wind from ERS scatterometer during 1993-2000 and from QuikSCAT during 2000-2006. The opposite signs of trends between the two periods indicate the presence of large decadal variability. The opposite signs of trends between the equatorial Pacific and Indian Oceans reflect the oscillation of the Walker Circulation on decadal time scales.

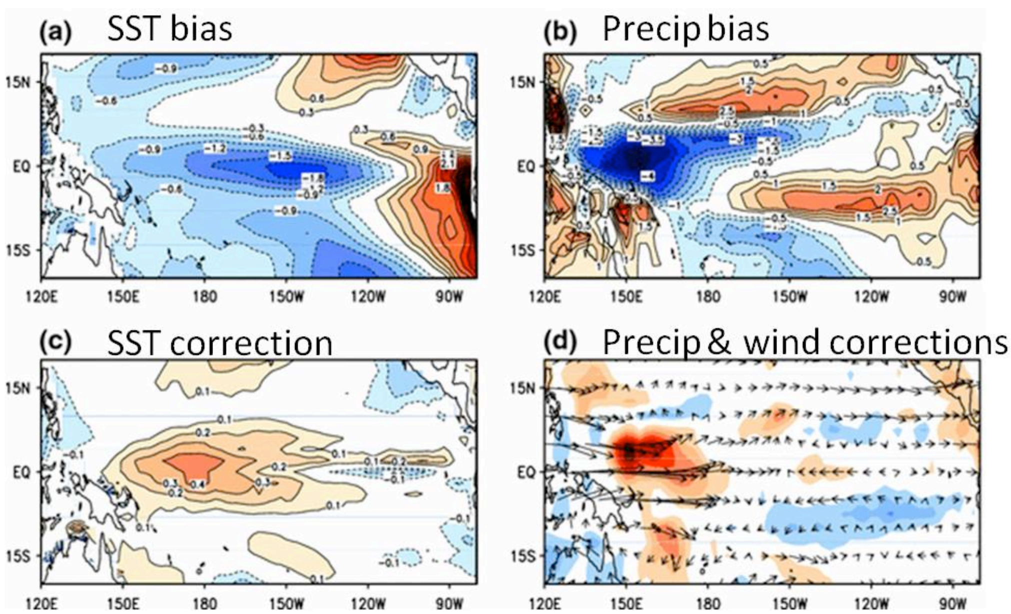

Figure 3.3: Climatological bias in SST (a) and precipitation (b) in the control run of the coupled GCM without diurnal coupling and the correction of SST (c) and precipitation and wind (d) due to the inclusion of diurnal coupling in the coupled model. After ham et al. (2010).

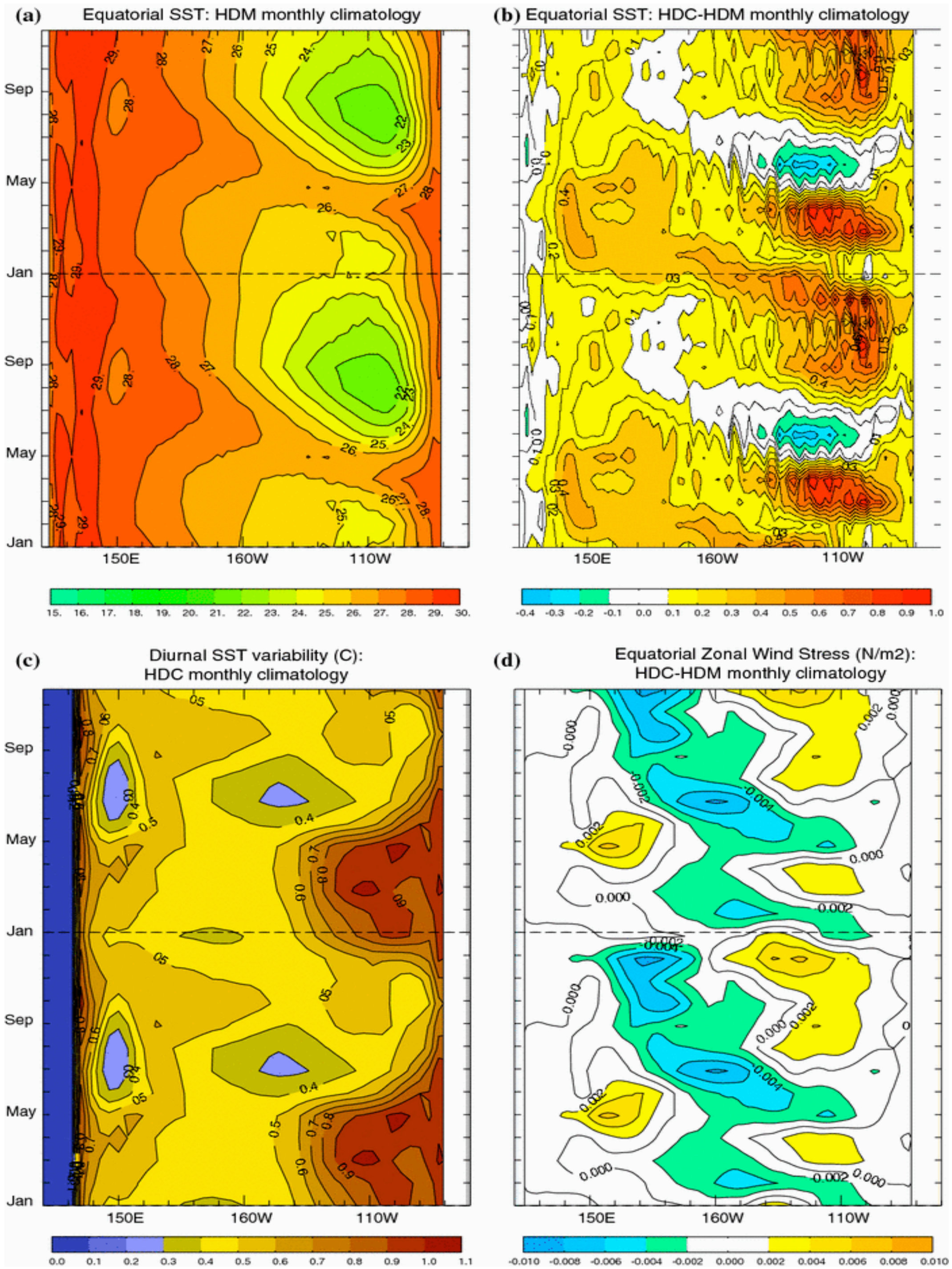

Figure 3.4: Climatological seasonal cycle across the equatorial Pacific: SST from the coupled model run without diurnal coupling (a), the difference in SST from model runs with and without diurnal coupling (b), diurnal SST variability the run with diurnal coupling (c), and difference in zonal wind stress from runs with and without diurnal coupling.

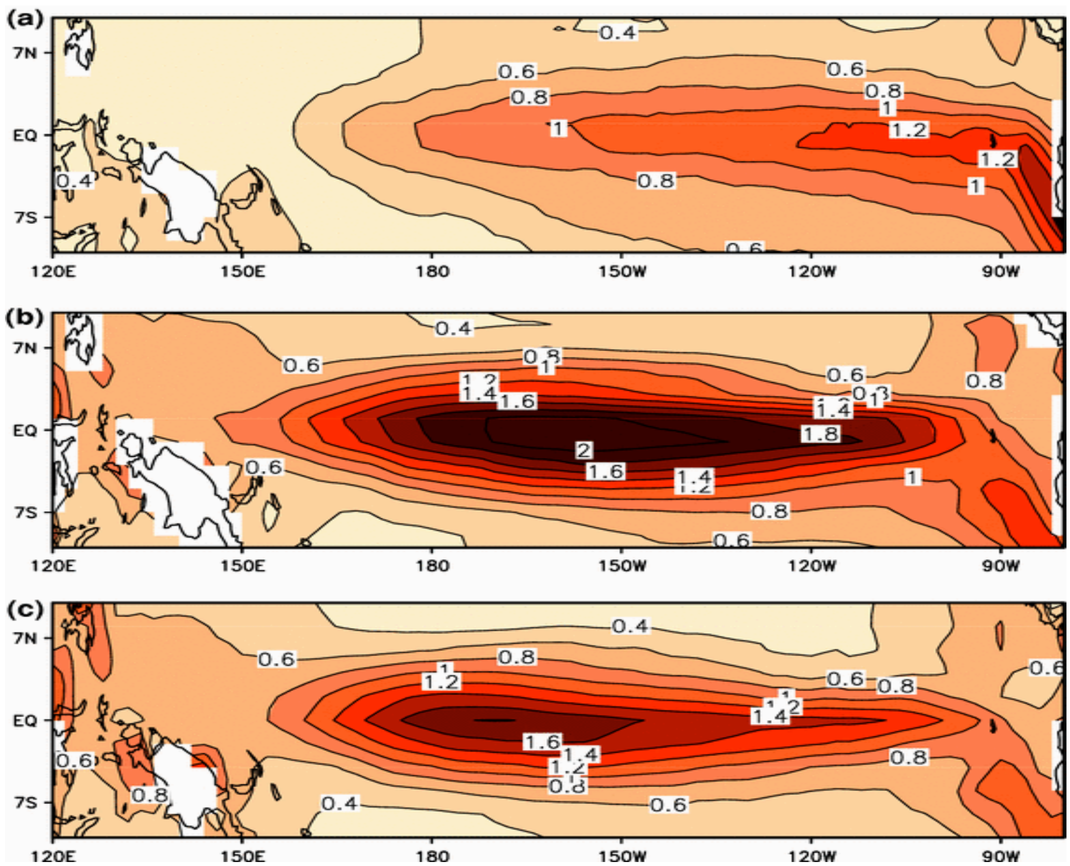

Figure 3.5: Standard deviation of interannual SST anomalies. (a) OISST data, (b) dialy coupling model run, and (c) diurnal coupling model run. After Ham et al. (2010).

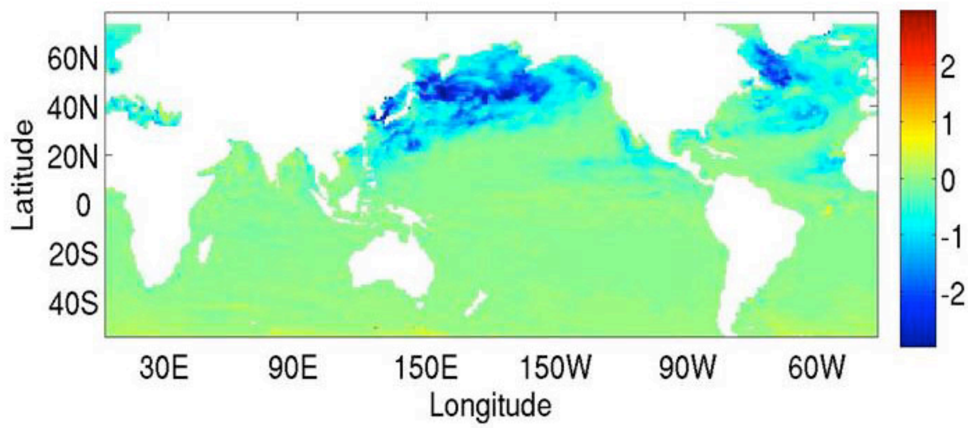

Figure 3.6: The difference of SST in August 2003 simulated by an ocean GCM forced by twice-daily and daily wind frocing obtained from the QuikSCAT-SeaWinds scatterometer tandem mission in 2003. The difference is due to stronger vertical mixing in the run with twice-daily wind because of more intense inertial oscillation generated by the twice-daily wind. After Lee et al. (2008).

An Example of the Impact of Assimilation of QuikSCAT Winds into the NCEP and ECMWF Models

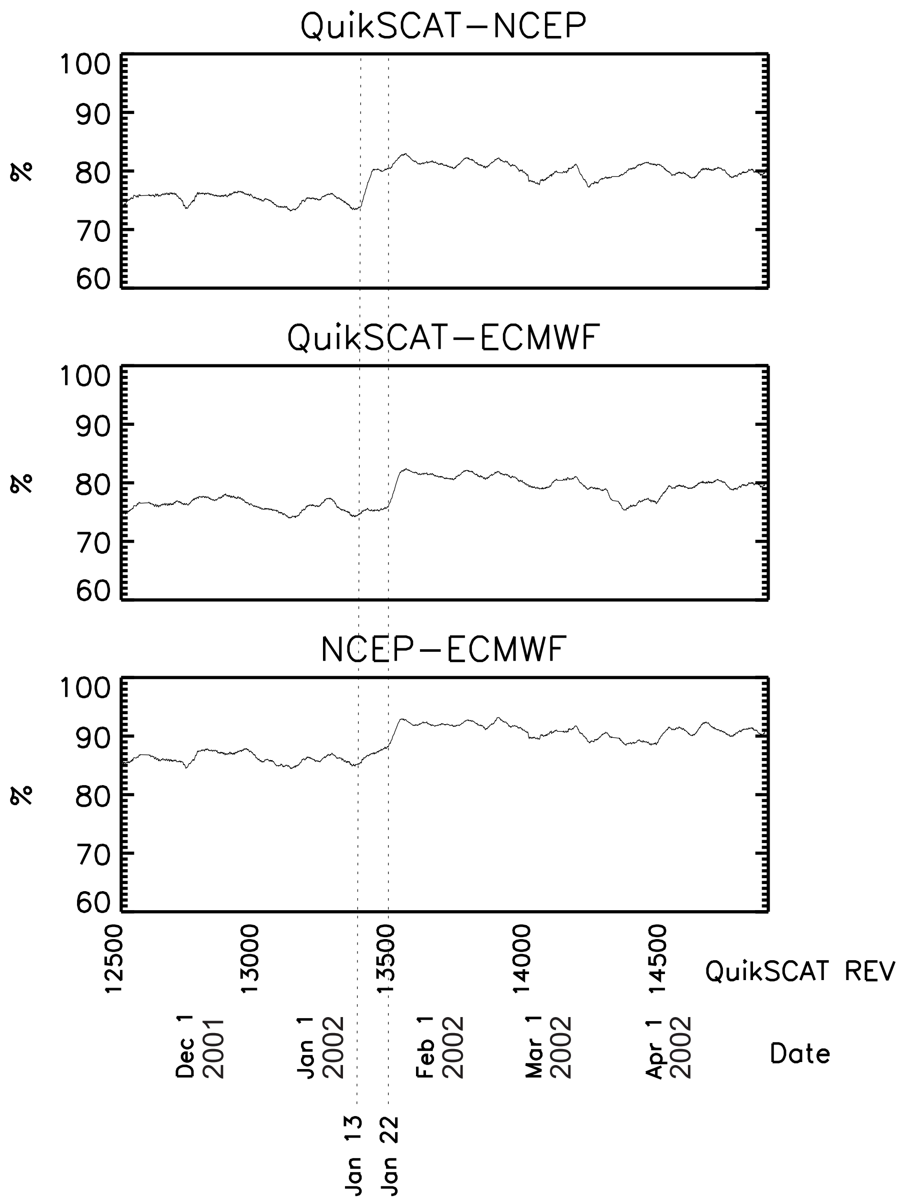

Figure 3.7: Daily time series of the percentages of collocated winds with directional differences less than 20o between 15 November 2001 and 1 March 2002. The NCEP and ECMWF models began assimilating QuikSCAT winds on 13 January 2002 and 22 January 2002, respectively. The top, middle and bottom panels correspond respectively to comparisons of QuikSCAT versus NCEP winds, QuikSCAT versus ECMWF winds, and NCEP versus ECMWF winds. Each time series was smoothed with a 4-day running average. (Chelton et al., 2006)

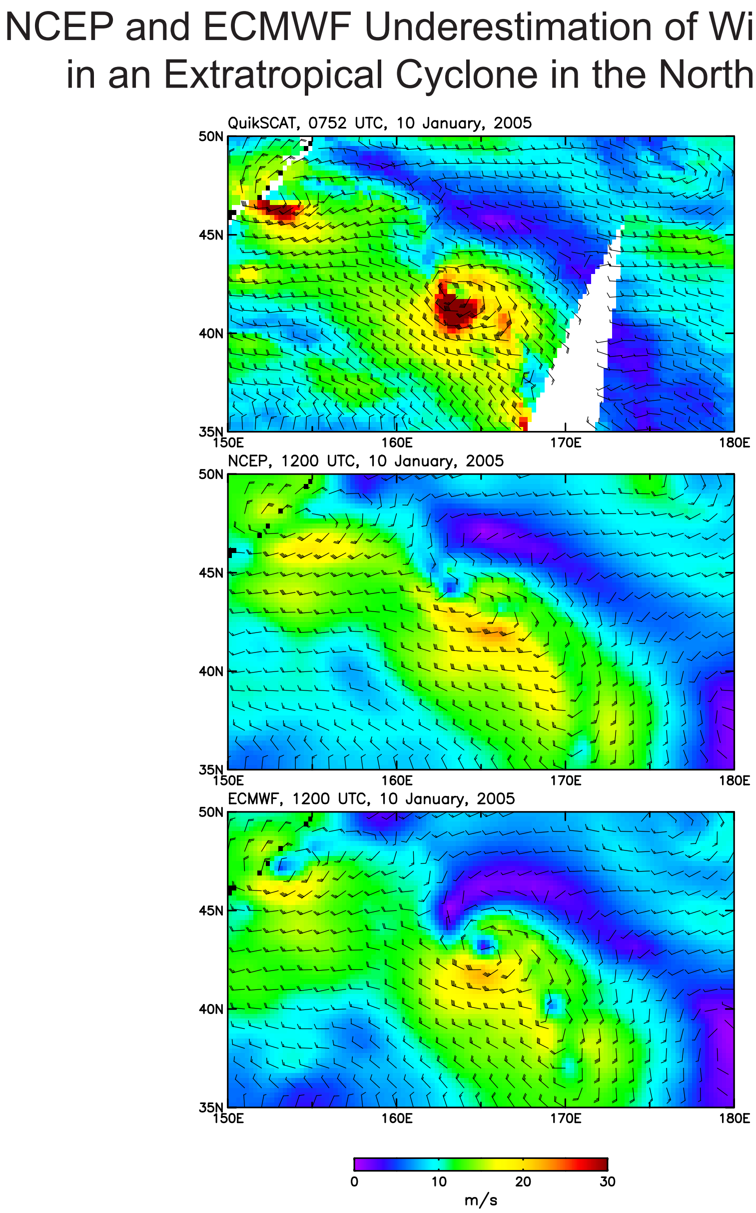

Figure 3.8: The wind fields in the western North Pacific on 10 January 2005 constructed for the times indicated on each panel from (top) QuikSCAT observations of 10-m winds, and from analyses of 10-m winds by (middle) the NCEP and (bottom) the ECMWF global numerical weather prediction models. Following meteorological convention, the wind barbs are in knots. The color scale corresponds to the wind speed in m s^{-1}. The QuikSCAT data were bin averaged in 0.25° latitude by 0.25° longitude areas. For clarity, the QuikSCAT wind vectors are plotted on a 0.75° by 0.75° grid. The NCEP and ECMWF wind vectors are plotted on a 1° by 1° grid. (Chelton et al., 2006)

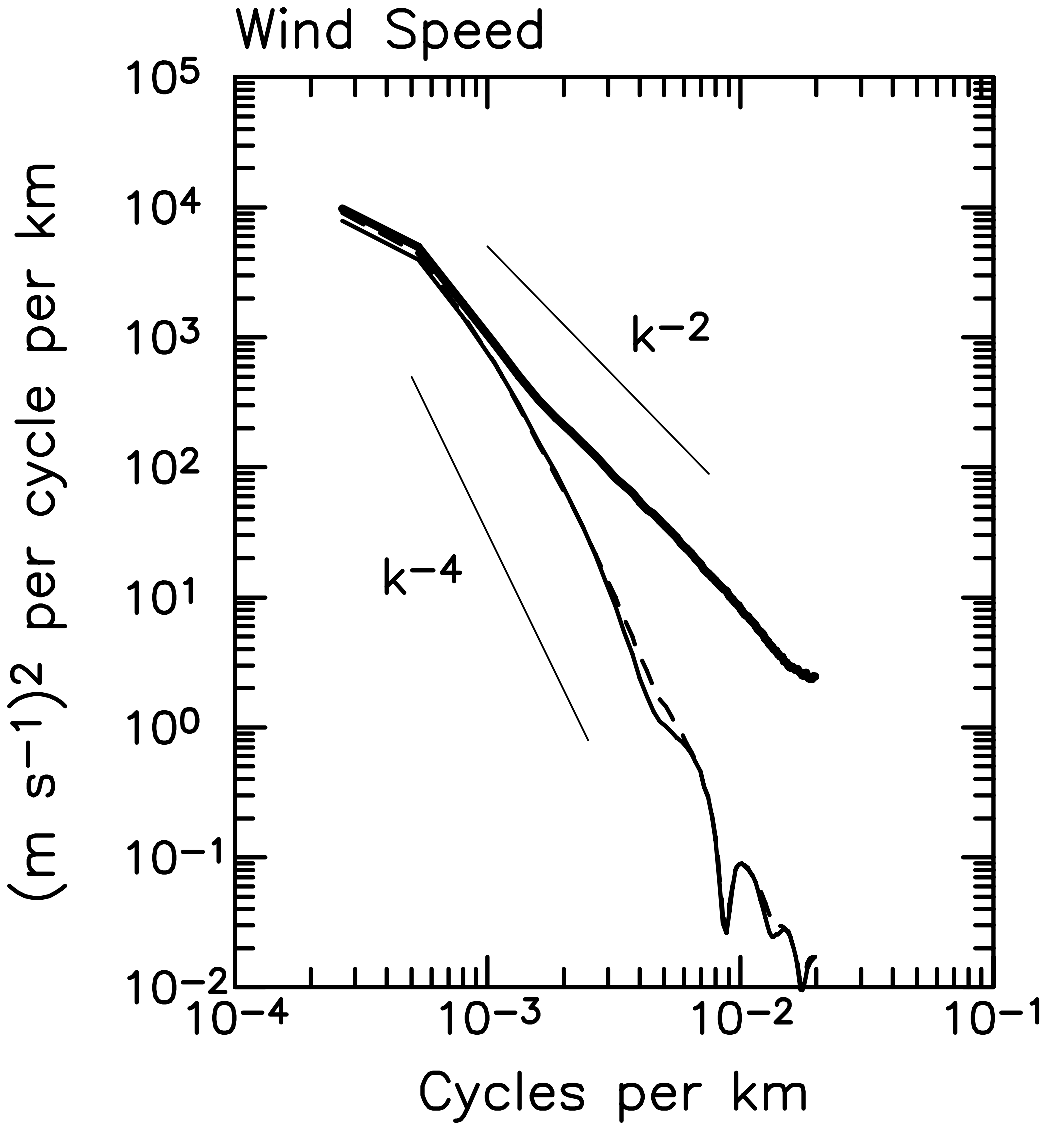

Figure 3.9: Along-track wavenumber spectra of wind speed in the eastern North Pacific computed from QuikSCAT observations (heavy solid lines), and from NCEP analyses (thin solid lines) and ECMWF analyses (dashed lines) of 10-m winds bilinearly interpolated to the times and locations of the QuikSCAT observations. The spectra from individual swaths were ensemble averaged over calendar year 2004. Lines corresponding to spectral dependencies of k^{-2} and k^{-4} on along-track wavenumber k are shown for reference. The structure at the highest wavenumbers in the wind speed spectra from NCEP and ECMWF is an artifact of the bilinear interpolation of the gridded wind fields to the QuikSCAT observation locations. (Chelton et al., 2006)

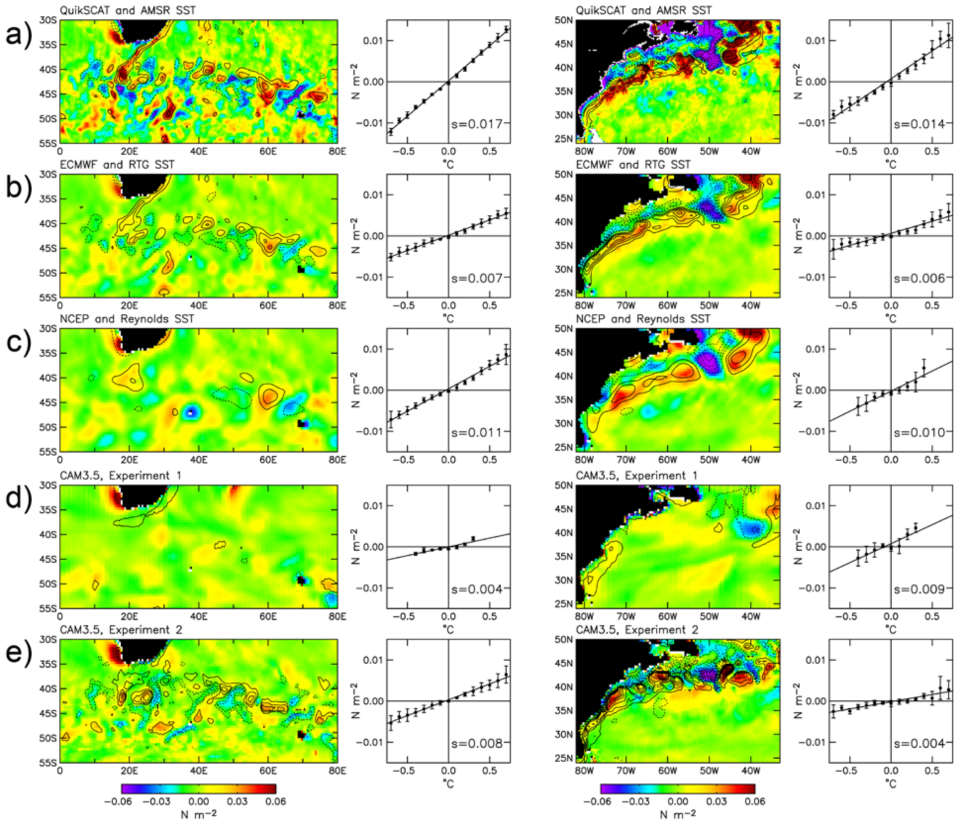

Figure 3.10: Maps and binned scatter plots for 2-month averages (January-February 2008) of spatially high-pass filtered SST overlaid as contours on spatially high-pass filtered wind stress magnitude for the Agulhas Return Current region (left) and the Gulf Stream region (right): a) QuikSCAT observations of wind stress and AMSR-E observations of SST; b) ECMWF wind stress and Real- Time Global (RTG) SST; c) NCEP wind stress and Reynolds SST; d) wind stress and SST from the NCAR CCSM3.5 coupled climate model with atmosphere and ocean grid resolutions of 0.5° and 1.125°, respectively; and e) wind stress and SST from the same NCAR CCSM3.5 coupled climate model with higher atmosphere and ocean grid resolutions of 0.5° and 0.1°, respectively. Positive and negative high-pass filtered SST is shown as solid and dotted lines, respectively, with a contour interval of 1°C and with the zero contours omitted for clarity. The CCSM3.5 model simulations are not intended to represent actual years, so the 2-month averages in panels d and e are for a representative January-February time period. The solid circles and error bars in the binned scatter plots are, respectively, the overall average and the standard deviation of the individual binned averages over eight January-February time periods for panels a-c and four January-February time periods for panels d and e. (Chelton and Xie, 2010)

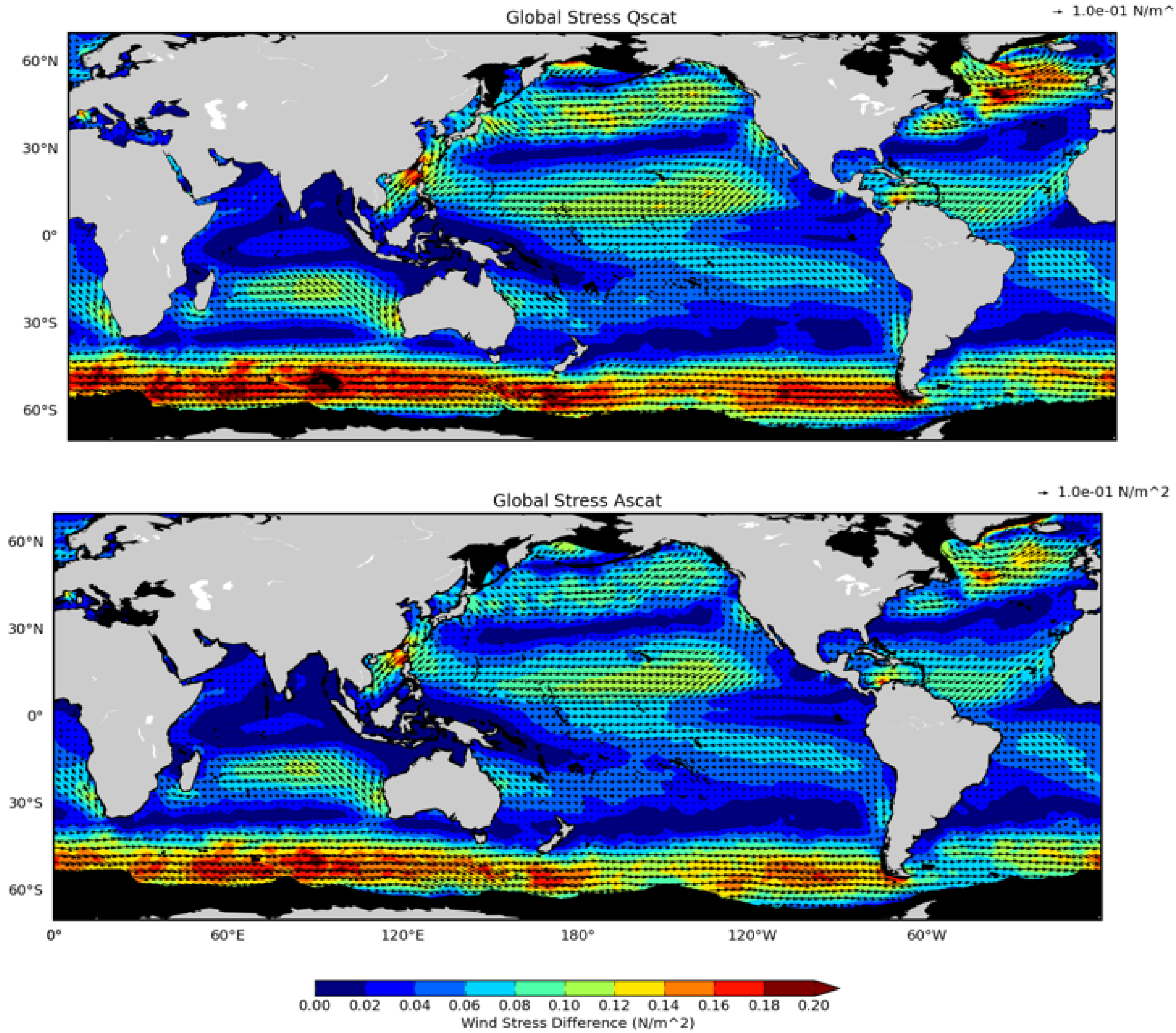

Figure 3.11: Wind stress climatologies derived from the save seven months of data from ASCAT and QuikSCAT. Although they agree in general, climatologia-clly important differences can be observed between the two data sets. Many of these differences are due to time of day differences, since there is approximately a 6 hour difference between the nominal data collection time between the two scatterometers. (Rodríguez and Veleva, JPL).

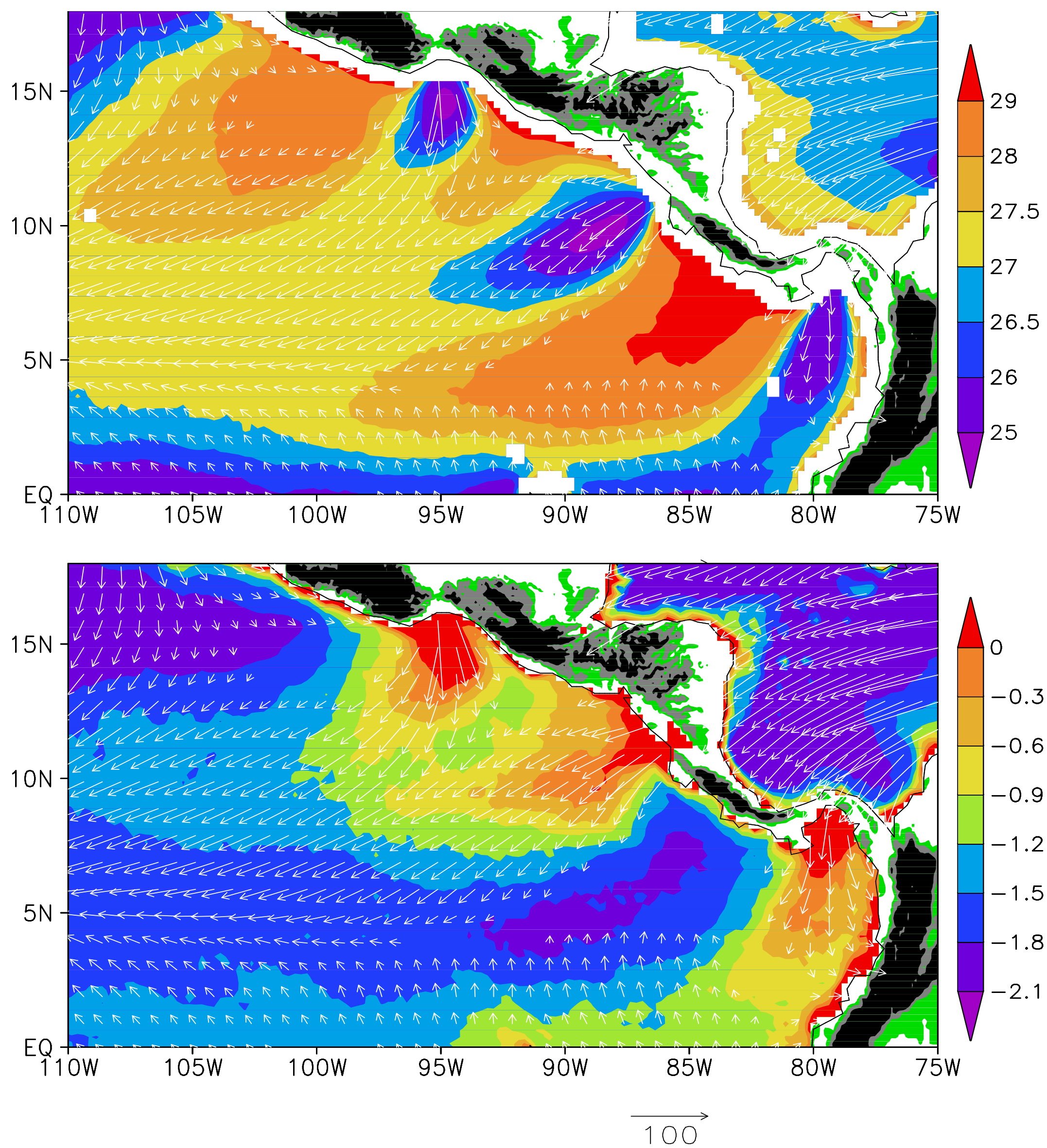

Figure 3.12: Jan–Mar climatology around Central America: QuikSCAT pseudo–wind stress (vectors; m^2 s^{-2}): (top) TMI SST (°C) and (bottom) SeaWiFS chlorophyll in natural logarithm (mg m^3). From Xie et al. (2005a).

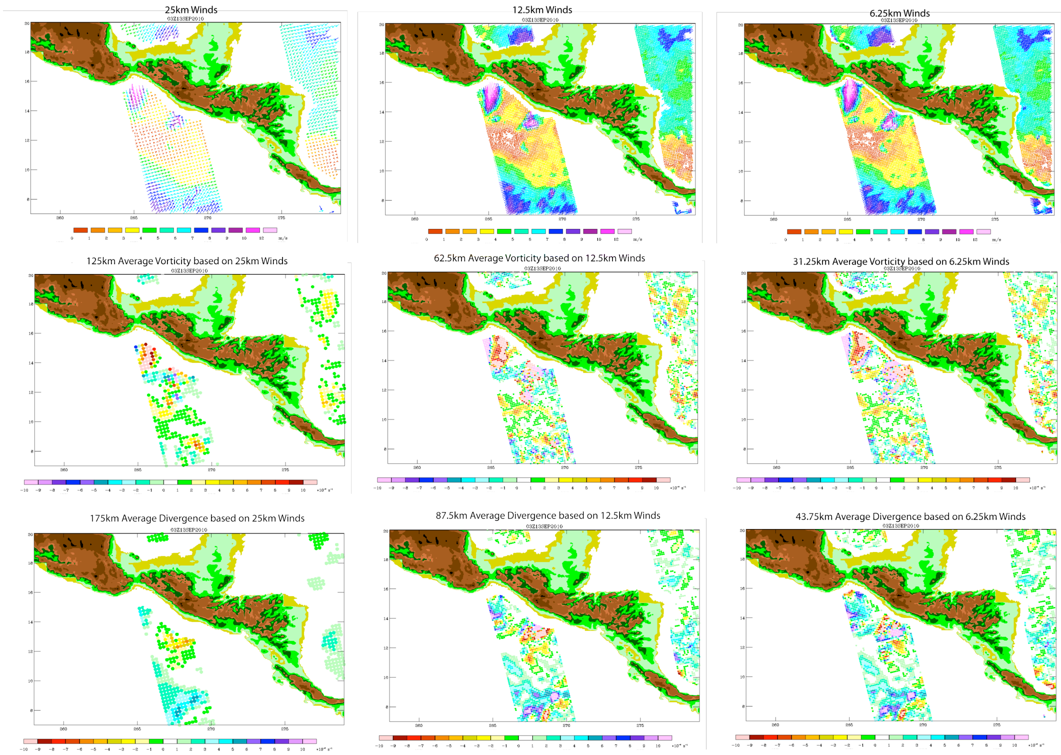

Figure 3.13: Wind Vectors (top row), vorticity (middle row), and divergence (bottom row) for 25 km ASCAT winds (left column), 12.5 km ASCAT winds (middle column), and 6.25 km ASCAT winds (right column). White areas indicate gaps between swaths and near zero values. The increased ASCAT resolution is achieved through filtering rather than actual improvements in resolution; therefore, these examples are expected to underestimate the advantages of finer resolution. The gap flow near Tehauntepec, Mexico and the near coastal wind gradients are much more evident in the finer resolution images. The vorticity (averaged of a roughly circular shape with a diameter of 5 grid cells to reduce noise) can be calculate much closer to the coast for the finer resolution products. The finest resolution vorticity images show a vorticity gradient near the coast, suggesting important ocean forcing is missed in the coarser resolution products, or could only be examined with a great deal of noise. The divergence is area averaged over a roughly circular shape with a diameter of seven grid cells to reduce noise. Again, the finer resolution divergence shows much clearer features. (Courtesy M. Bourassa).

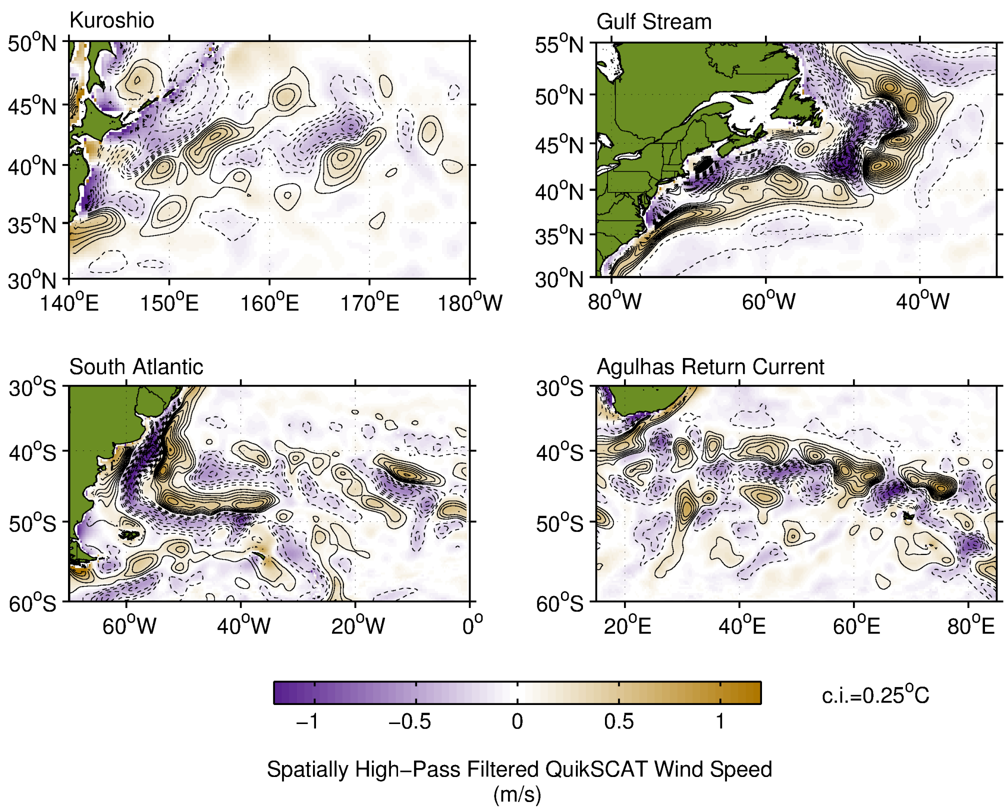

Figure 3.14: Maps of spatially high-pass filtered QuikSCAT wind speed (colors) with contours of spatially high-pass filtered AMSR-E SST overlaid. Solid contours are warm SST perturbations and dashed are cool SST perturbations, and the contour interval is 0.25°C. The satellite data used in these maps are averaged over the 7-year period June 2002-May 2009. (O'Neill et al., 2012)

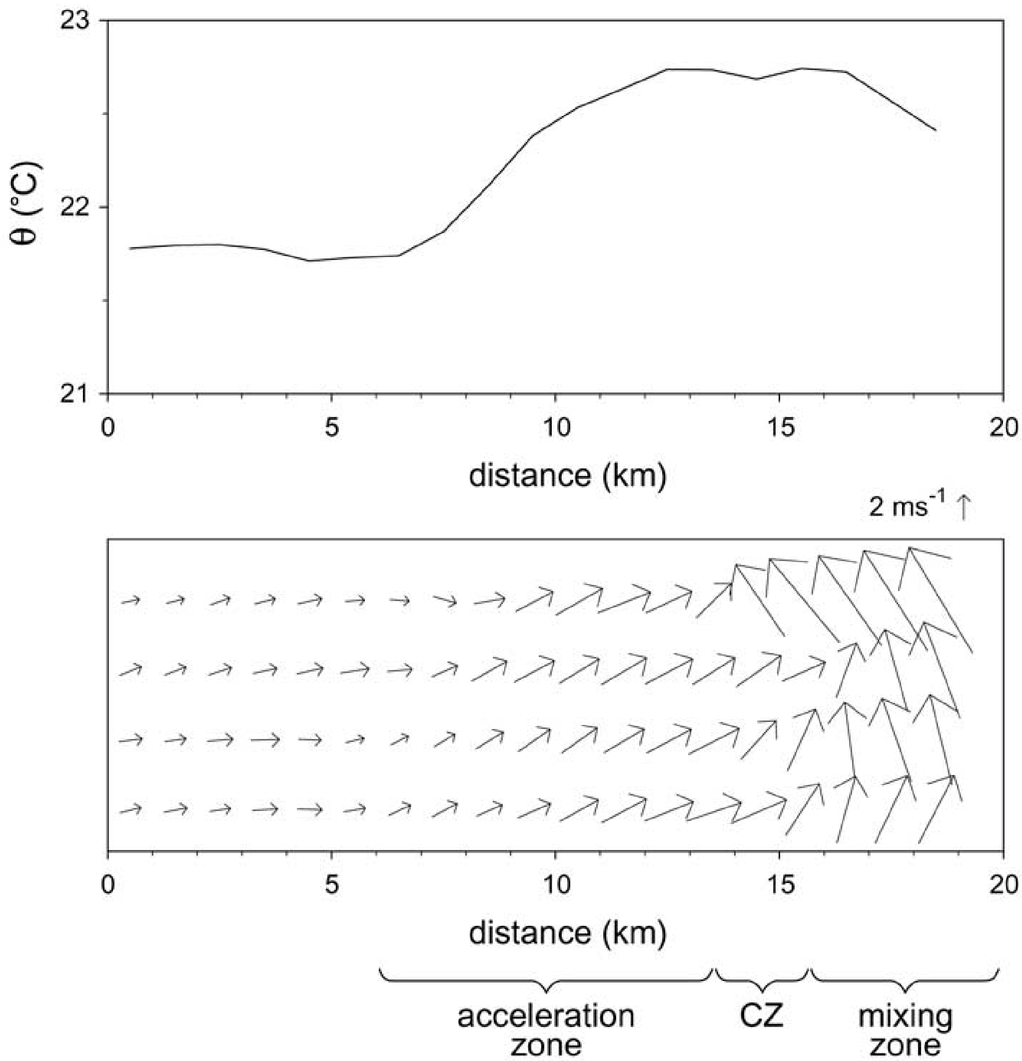

Figure 3.15: The along-flight variation of the composited potential temperature at the 33-m level on 20 November (upper panel) and the 1-km averaged wind vectors at 33 m (lower panel) for four sequential passes over the same track. The vectors are plotted as a planview with north directed upward and east directed to the right. The bracketing delineates the zone where the flow is accelerated toward the warmest air, the convergence zone (CZ) and the zone where strong southerly momentum is convectively mixed downward toward the surface. (From Mahrt et al. (2004)).

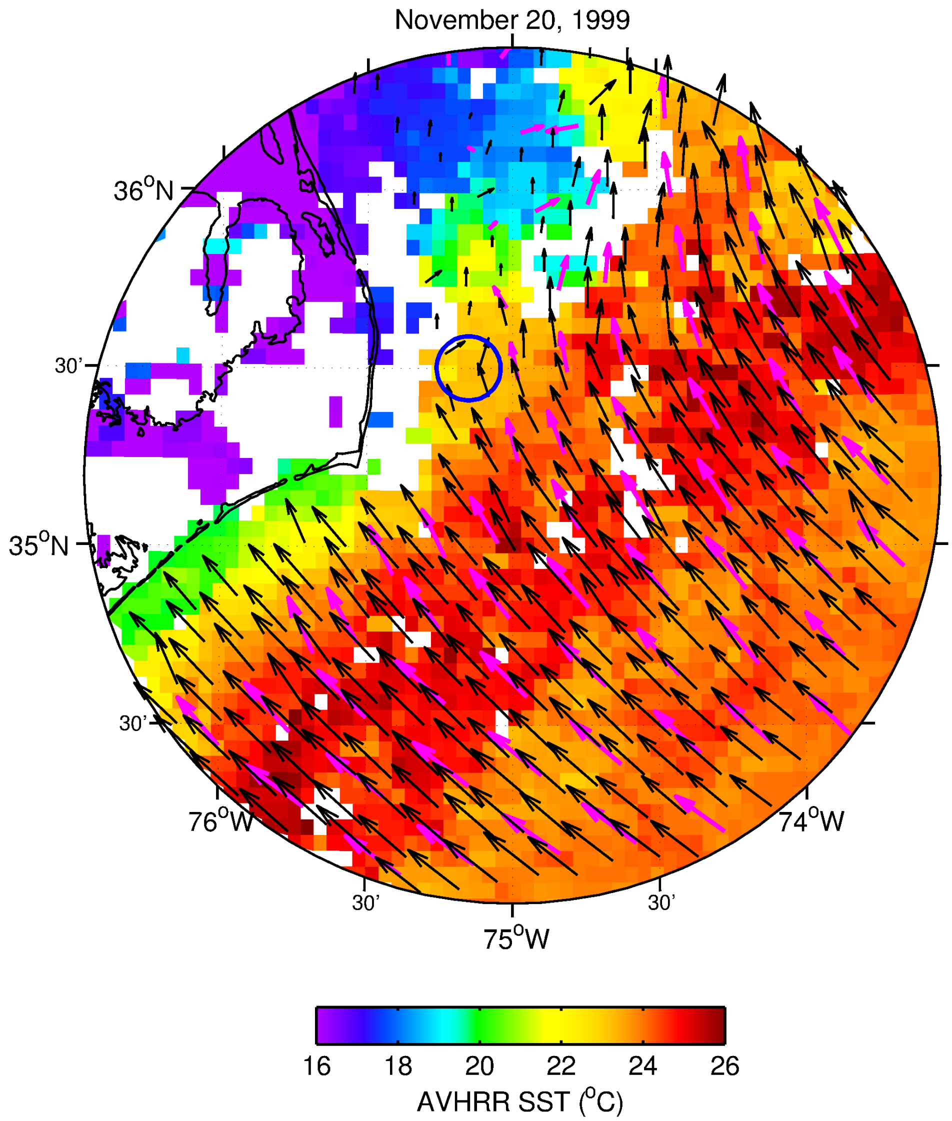

Figure 3.16: A map of the 10-day averaged AVHRR SST (colors) with QuikSCAT wind vectors overlaid at a spatial resolution of 25 km (magenta) and 12.5 km (black) on Nov. 20, 1999. The region enclosed by the blue circle is the approximate region where the aircraft observations shown in Figure 3.15 were collected. The warm water associated with the Gulf Stream runs diagonal across this figure from southwest to northeast.

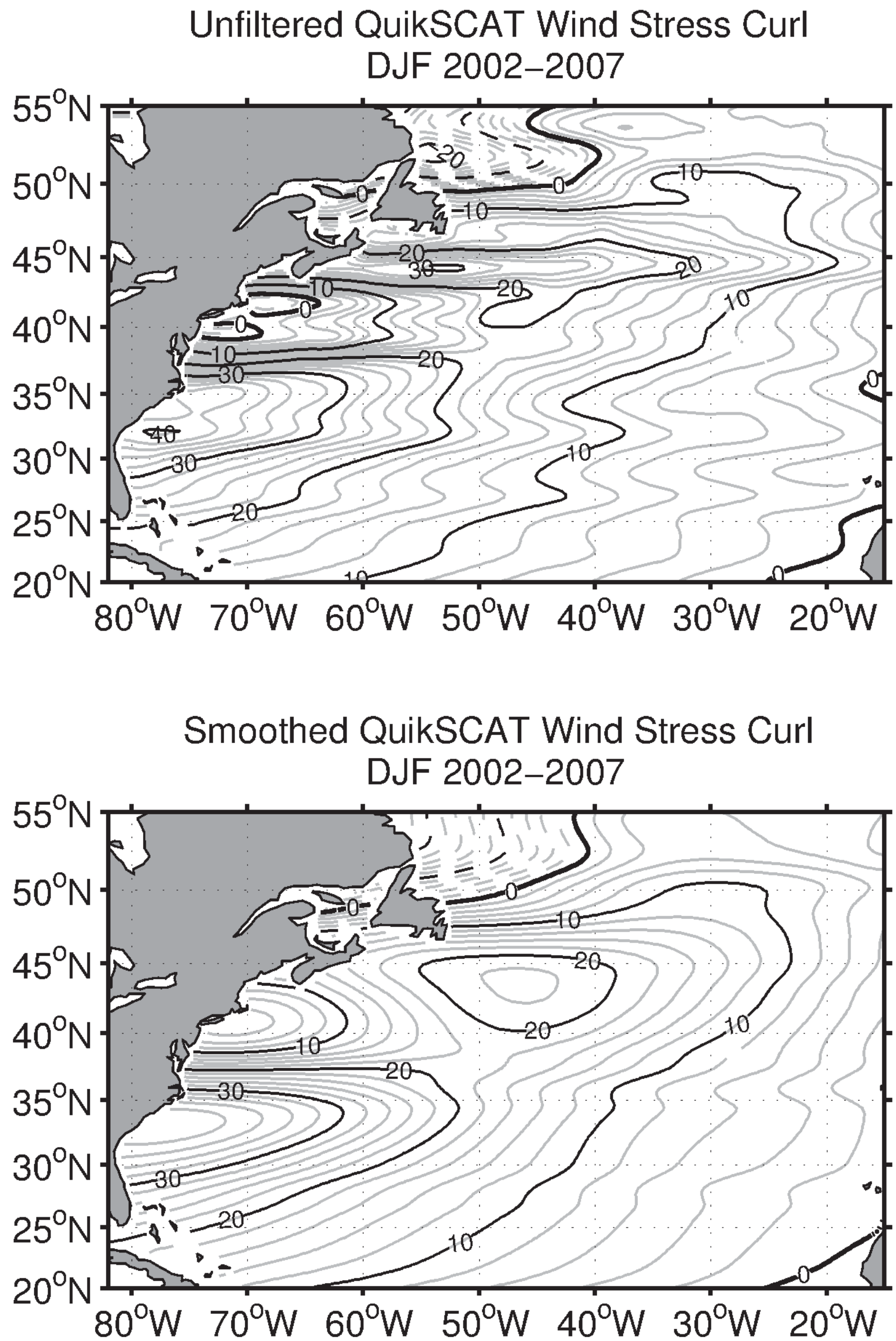

Figure 3.17: Sverdrup volume transport streamfunction over the north Atlantic computed from the (top row) unfiltered and (bottom row) spatially low-pass filtered QuikSCAT wind stress curl fields over the time periods as indicated below each column of panels. The contour interval is 2 Sverdrups (Sv), and the positive contours are solid while the negative contours are dashed.

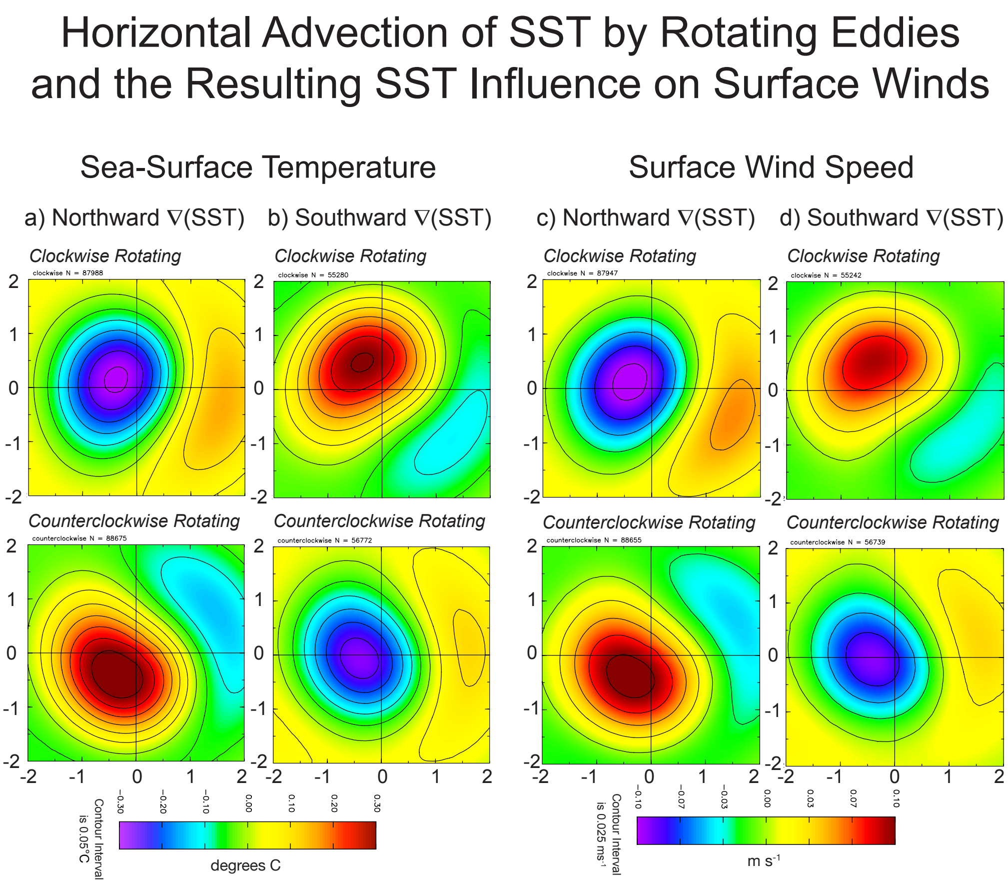

Figure 3.18: Composite averages of filtered fields in a rotated coordinate system (see explanation in the caption for Figure 3.19) collocated to the interiors of CW (top panels) and CCW (bottom panels) rotating eddies. The radial distance in each eddy was normalized by its radius of maximum rotational speed. The pairs of panels correspond to: a) SST globally between 15° and 45° latitude in regions with a northward component of SST gradient; b) SST globally between 15° and 45° latitude in regions with a southward component of SST gradient; c) wind speed globally between 15° and 45° latitude for the same eddies included in the SST composites in panel a); and d) wind speed globally between 15° and 45° latitude for the same eddies included in the SST composites in panel b). (Courtesy P. Gaube and D. Chelton, Oregon State University)

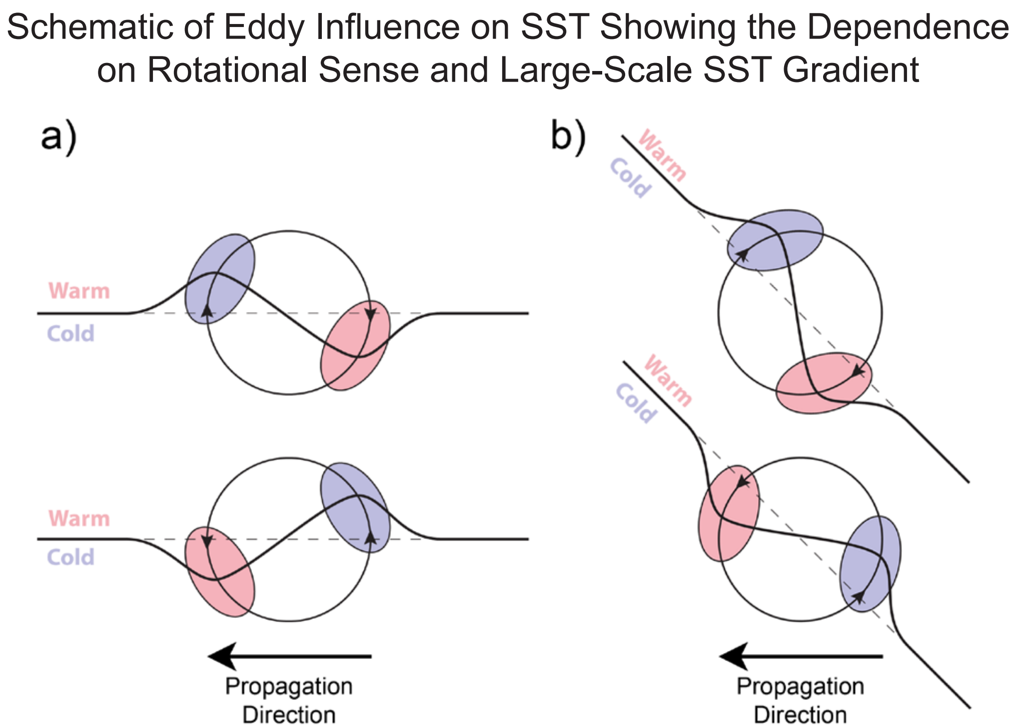

Figure 3.19: Schematic diagram of eddy-driven horizontal advection of SST for CW and CCW rotating eddies (top and bottom, respectively) propagating westward in regions where the SST gradient is: a) northward; and b) northeastward. An otherwise smooth contour of SST (dashed lines) is distorted by the rotational velocity field within the eddy, as shown by the solid lines. Advection of SST within the large-scale background SST gradient results in the positive and negative SST anomalies shown by the red and blue regions, respectively. The dependence of the locations of these SST anomalies on the direction of the large-scale background SST gradient that is evident from comparison of a) and b) was accounted for by composite averaging in a coordinate system rotated for each eddy so that the SST gradient vector is oriented at a polar angle of 90° or –90°, depending on whether the ambient SST gradient has a northward or southward component, respectively.(Chelton et al., 2011)

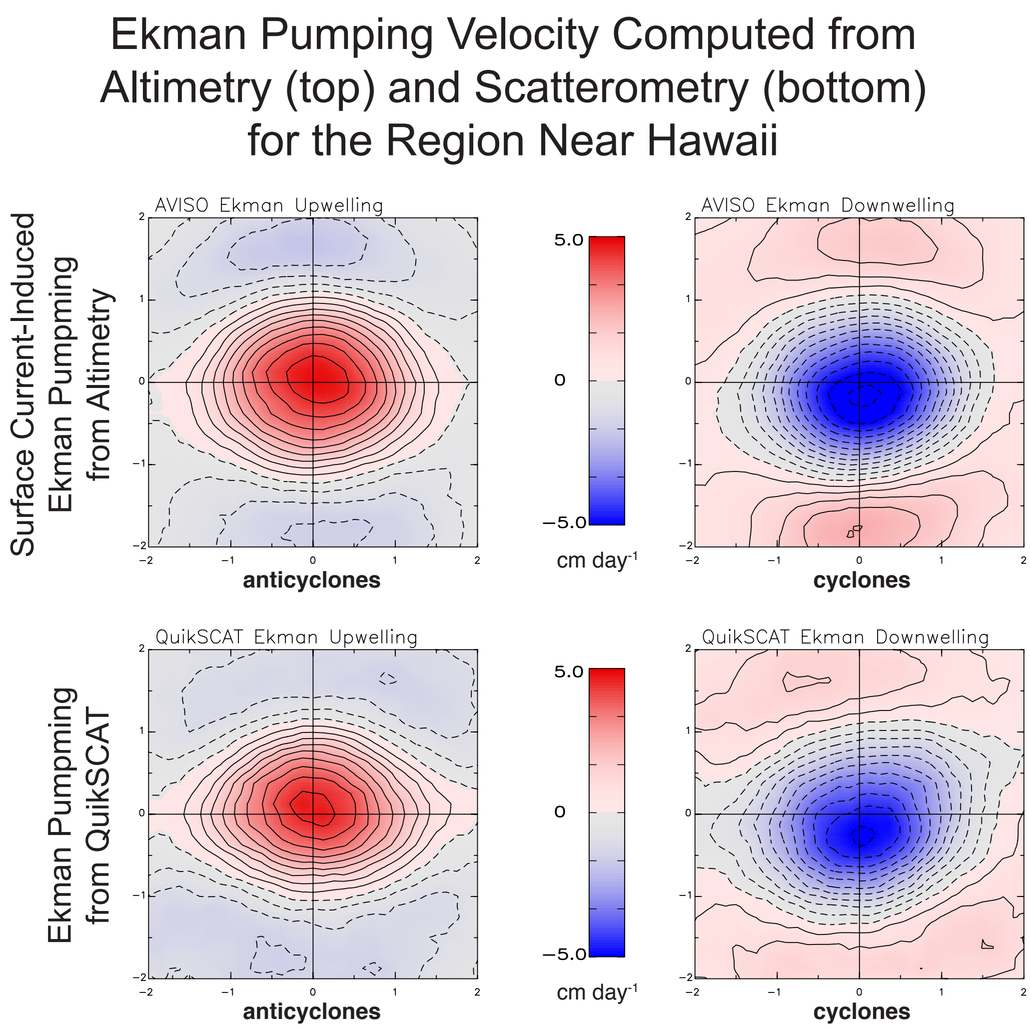

Figure 3.20: Composite averages of Ekman pumping velocity from the surface geostrophic velocity computed from filtered SSH fields (top panels) and from filtered QuikSCAT wind stress fields (bottom panels) collocated to the interiors of anticyclones and cyclones (left and right panels, respectively) for the region 15°N–25°N, 180°W–140°W centered on the Hawaiian Islands. (Courtesy P. Gaube and D. Chelton, Oregon State University)

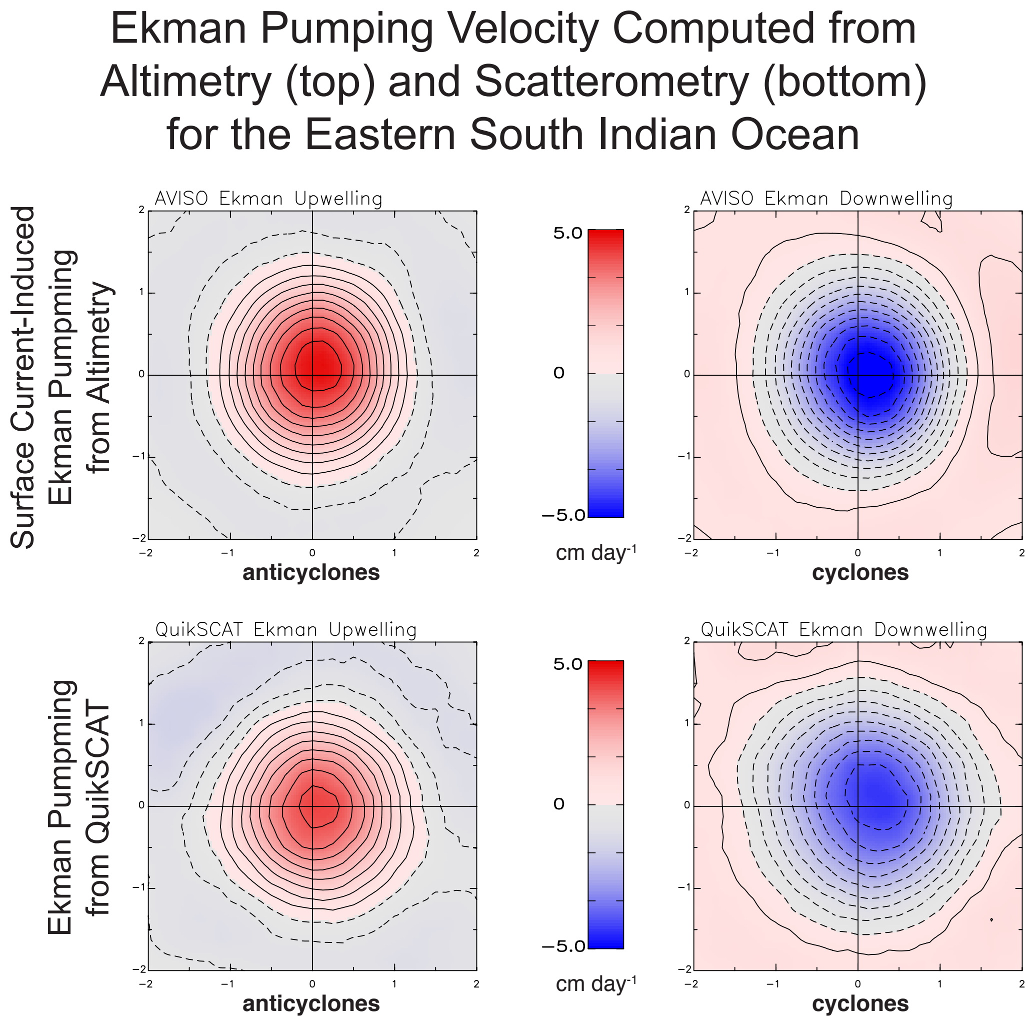

Figure 3.21: The same as Figure 3.20, except for the region 35°S–20°S, 80°E–120°E of the eastern South Indian Ocean. (Courtesy P. Gaube and D. Chelton, Oregon State University)

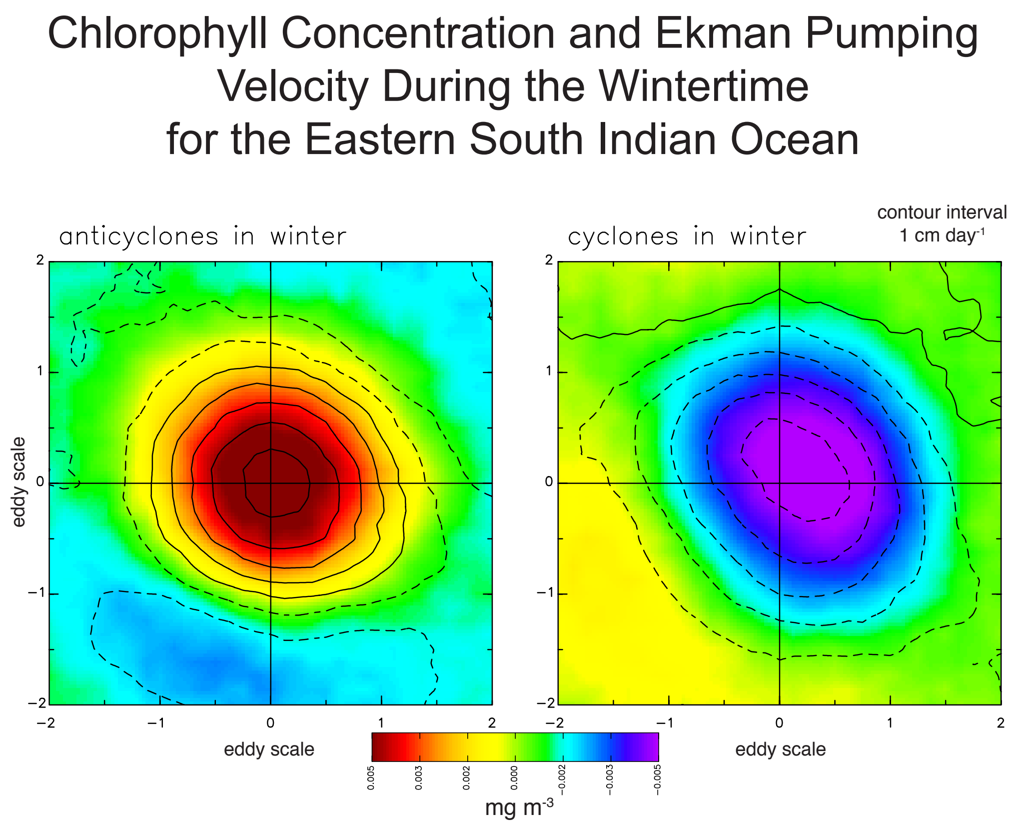

Figure 3.22: Composite averages of filtered fields of chlorophyll (color) and Ekman pumping velocity (contours) collocated to the interiors of anticyclones (left) and cyclones (right) during austral wintertime in the region 35°S–20°S, 80°E–120°E of the eastern South Indian Ocean. (Courtesy P. Gaube and D. Chelton, Oregon State University)

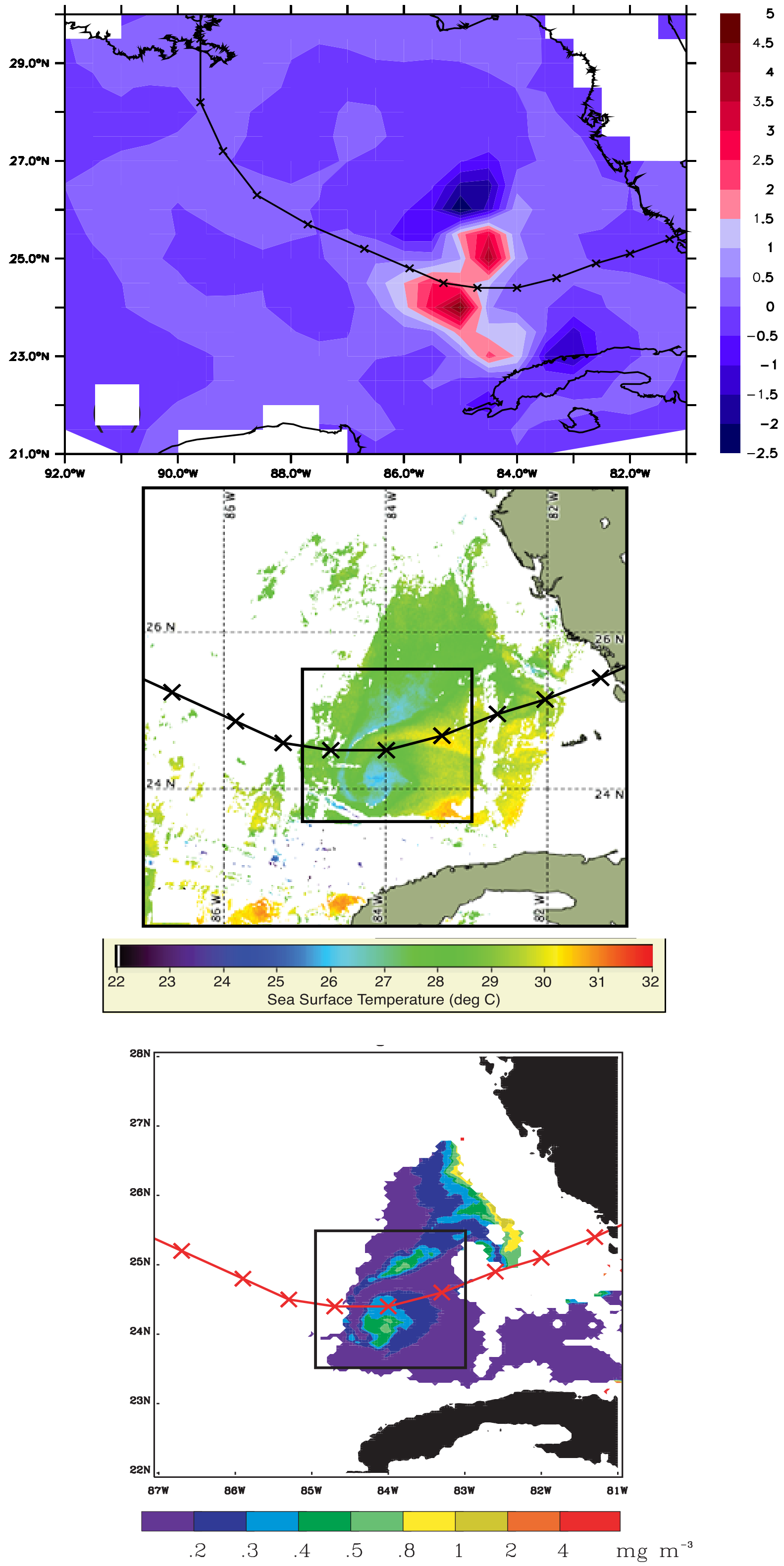

Figure 3.23: (upper) QuikSCAT-derived Ekman pumping (10-4 m s-1) during Hurricane Katrina at 1200 UTC 27 August 2005, (middle) AVHRR SST (°C) and (lower) MODIS chl-a (mg m-3) on 30 August 2005, 3 days after passage of Katrina. (Gierach and Subrahmanyam, 2008)

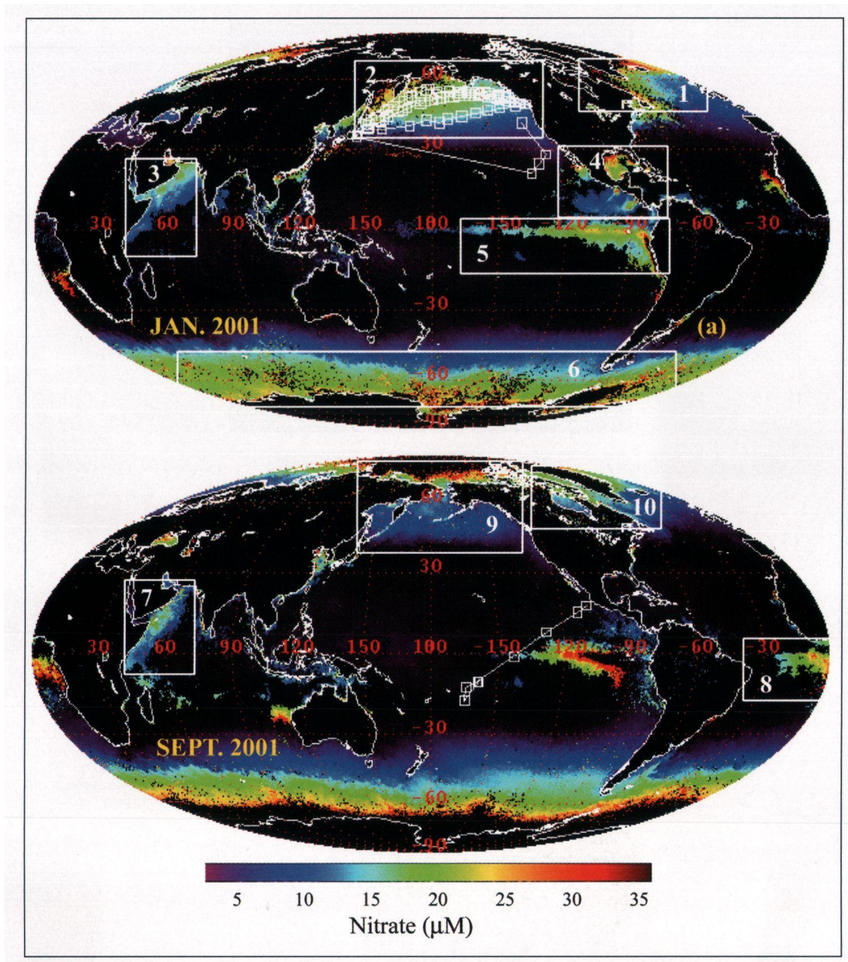

Figure 3.24: Global images of surface nitrate concentrations generated using MODIS Terra SST and chl-a for (upper) January 2001 and (lower) September 2001. (Goes et al., 2004).

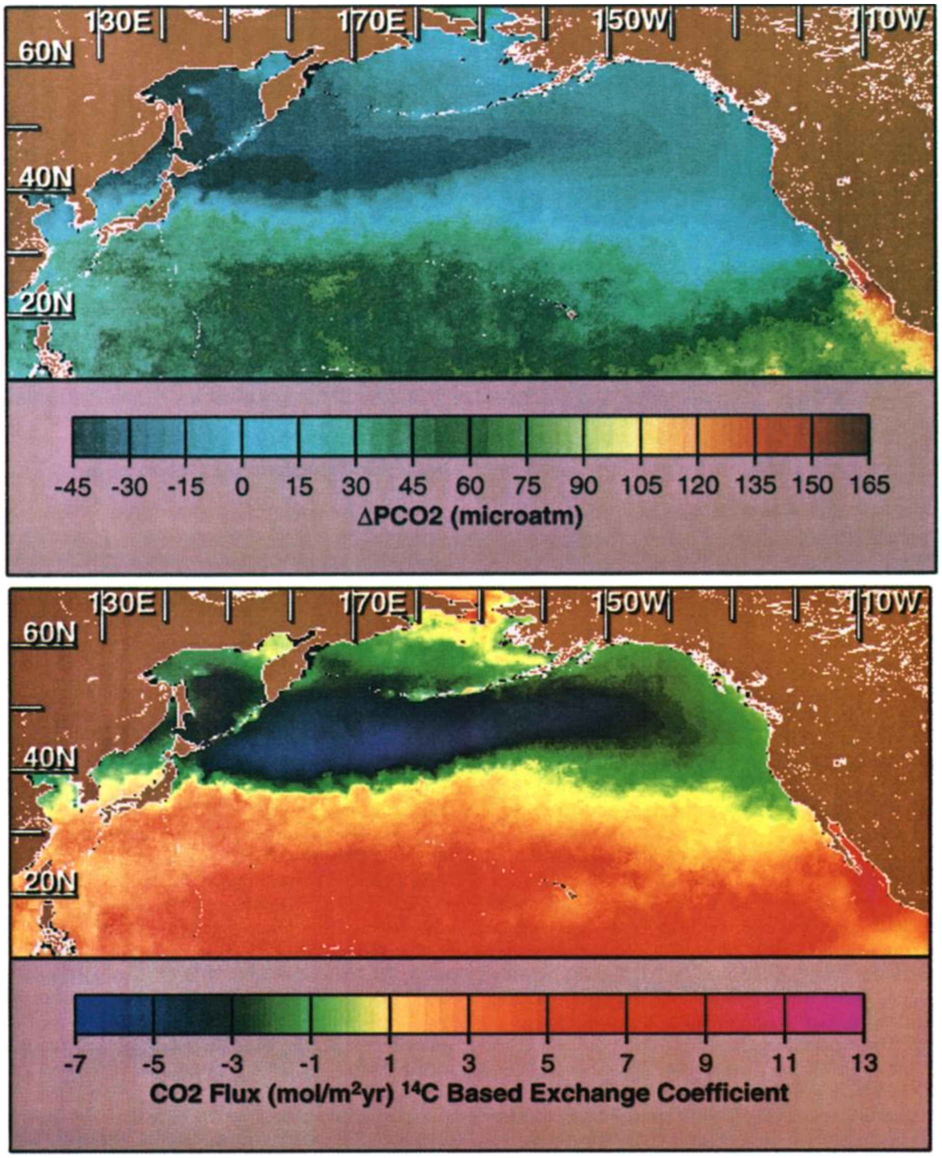

Figure 3.25: Map of (upper) ΔpCO2 and (lower) sea-air CO2 flux in the North Pacific for September 1985. Seawater pCO2 values are calculated from satellite SST. The flux is calculated from the satellite-derived ΔpCO2 maps and ECMWF winds. (Stephens et al., 1995)

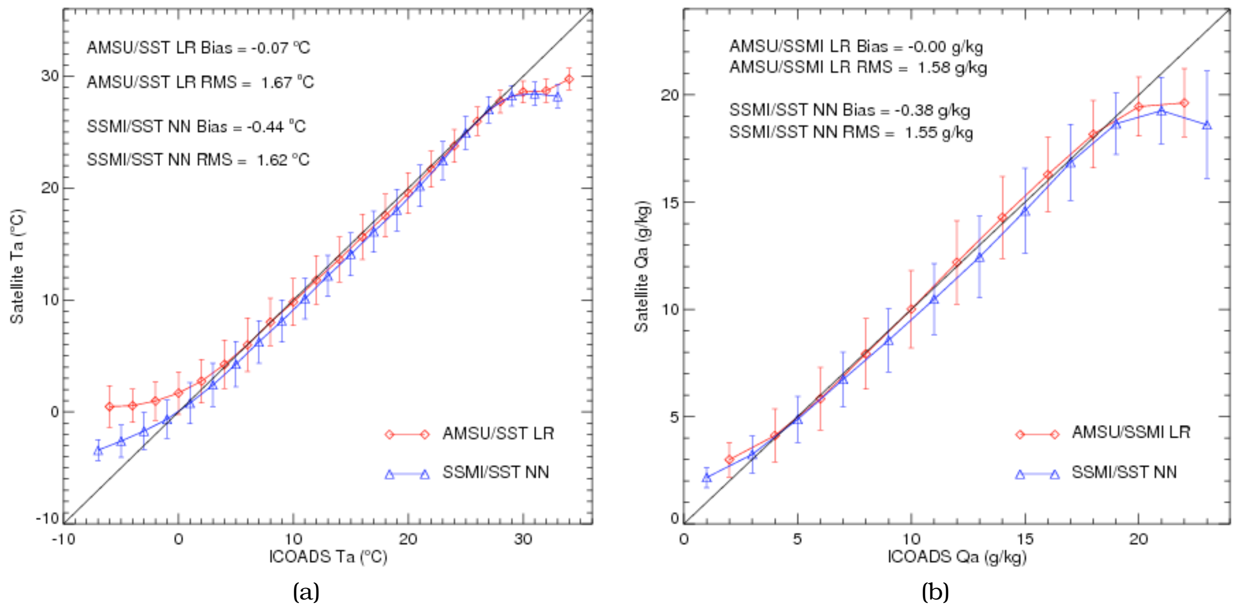

Figure 3.26: Scatter plot of 10m air temperature (left) and 10m humidity (right) from ICOADS (in situ) versus satellite-derived. The red-curve represents the Jackson et al. (2009) multiple linear regression retrieval technique. The blue curve represents the Roberts et al. (2010) neural network retrieval technique. Both perform well overall, but have biases near the extremes due to a lack of training data. (Courtesy M. Bourassa, FSU)

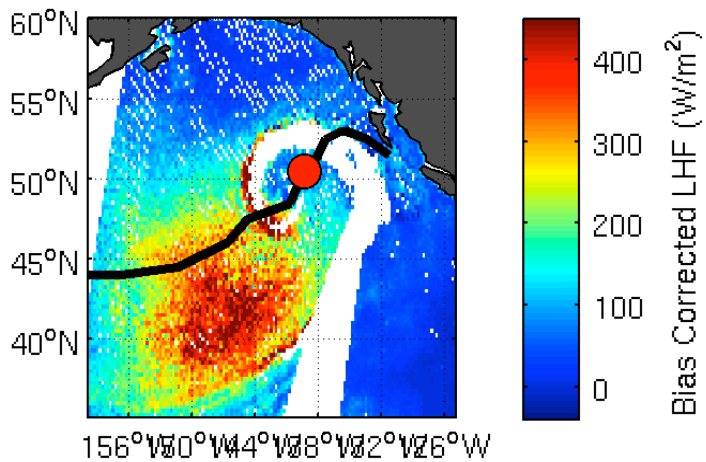

Figure 3.27: Example of latent heat fluxes from an intense mid-latitude cyclone. The black line indicates storm track from Ryan Maue's MERRA-based algorithm, and the red dot is the center of the cyclone. The large area of high fluxes is behind a cold front, with strong winds blowing over relatively warm water. The white areas indicate either unobserved areas between swaths or heavily rain contaminated areas. (Courtesy M. Bourassa, R. Maue, FSU).

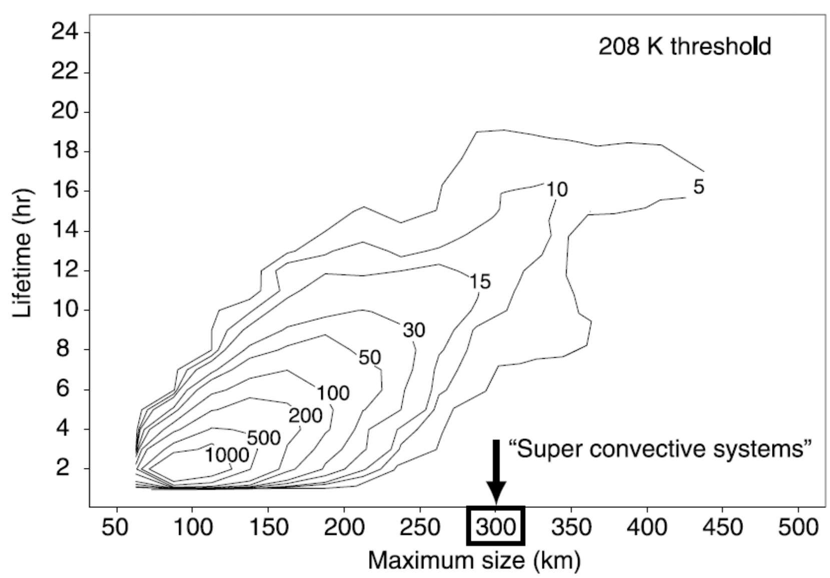

Figure 3.28: Timescales and space scales of MCSs in TOGA COARE. MCSs were defined by a cloud top temperature threshold of 208 K and by whether they exhibited continuity in both space and time. Frequency distribution shows occurrences of tracked MCSs (number per 25-km-size interval per hour) as a function of the maximum size (abscissa) reached by a convective system during its lifetime (from start to end of its life cycle). From Houze (2004).

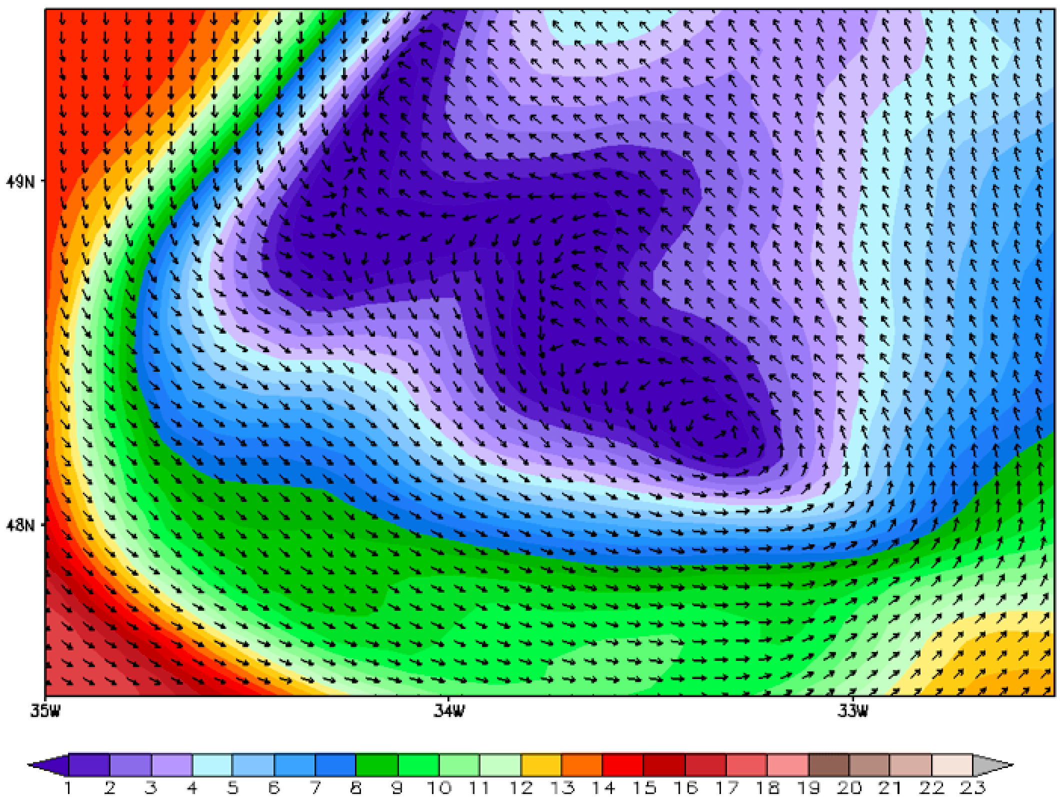

Figure 3.29: WRF simulation of the core of an intense mid-latitude cyclone, with wind vectors shown every 5km, and the wind speeds (ms^{-1}) shown on the color bar. The 5 km winds are desired for the circulation in the center of the storm and for the atmospheric fronts (not shown); however, 15 km winds are excellent for most other conditions. (Courtesy M. Bourassa)

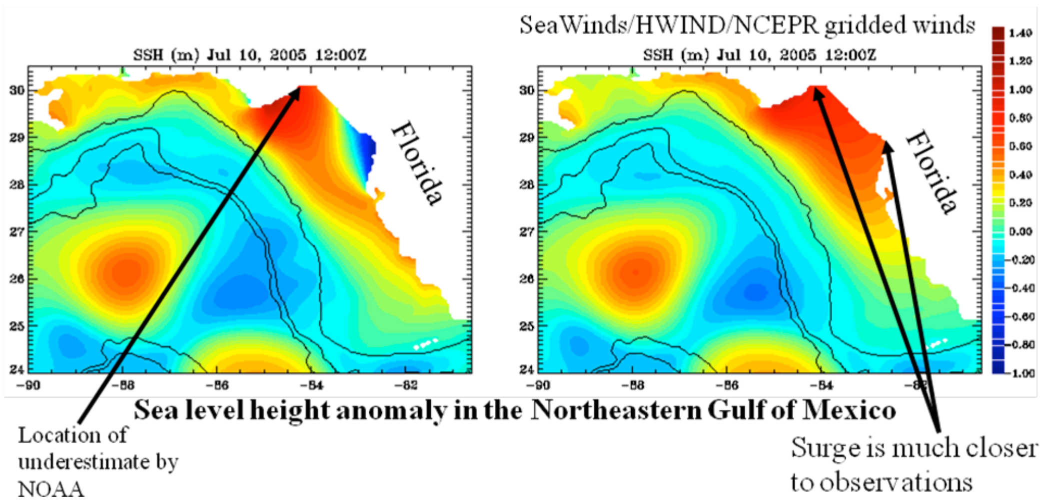

Figure 3.30: Modeled storm surge with low spatially and temporally low resolution winds from a combination of SeaWinds (when available) and NCEP Reanalysis II winds (left) and the same data combined with the NCEP/HRD H*Wind product (right). The storm surge on the right is much closer to observations.

Figure 3.31: Cartoon of radiometer (upper) and radar (lower) measurement geometries. The radiometers integrates all the information along the antenna beam, while the radar integrates all the information arriving at the same time in a radar pulse. The two sets of data contain complimentary information. (Courtesy Z. Haddad, JPL/CalTech)

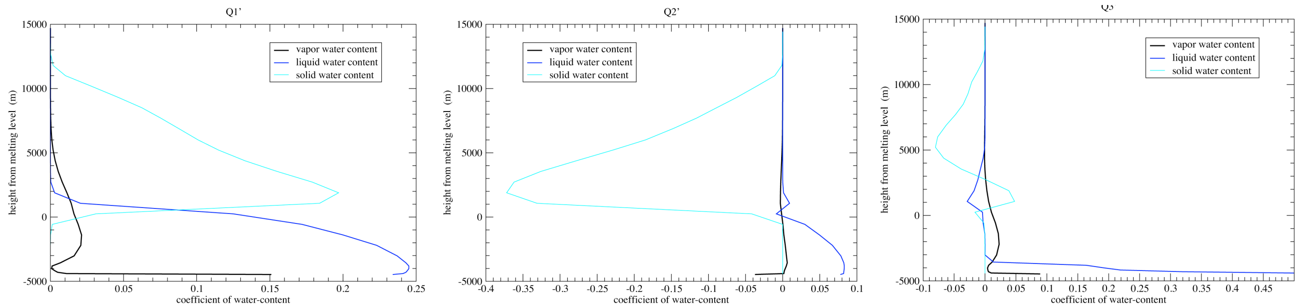

Figure 3.32: Coefficients of the first 3 principal components of the condensation, derived from 18 cloud resolving simulations of tropical cyclones. (Courtesy Z. Haddad, JPL/CalTech)

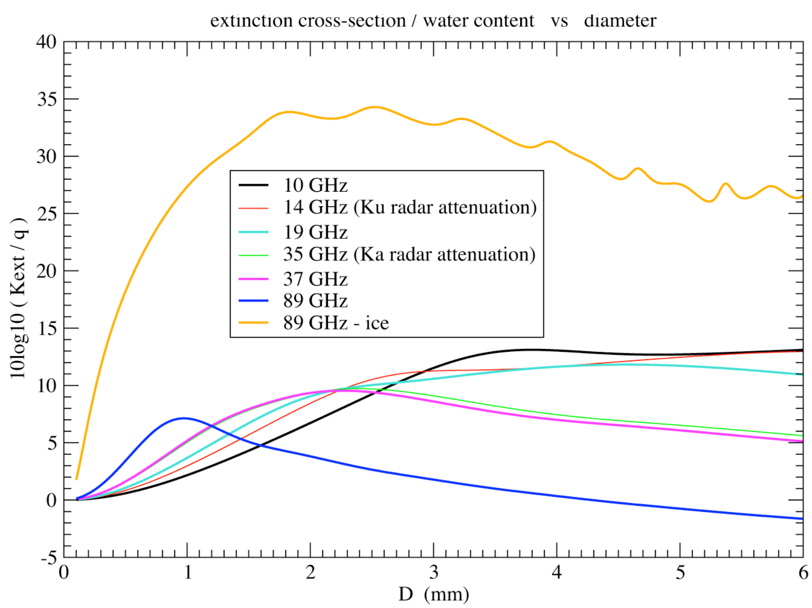

Figure 3.33: Passive signatures, showing the increased absorption at Ka band versus Ku band, and the strong scattering signature of ice at W band. (Courtesy Z. Haddad, JPL/CalTech)

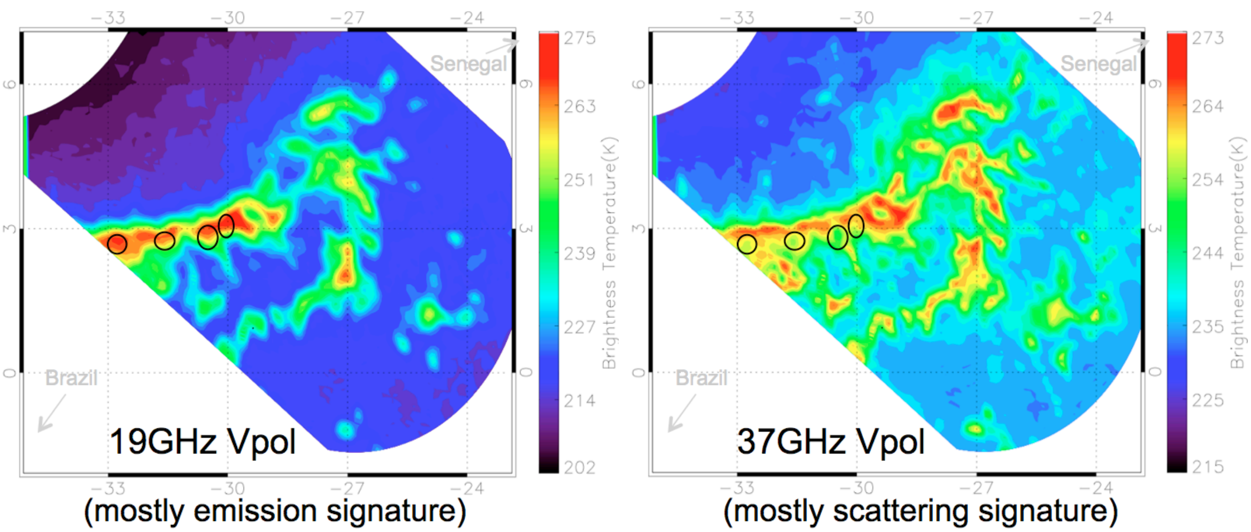

Figure 3.34: Warmer brightness temperatures at 19 GHz and colder temperatures at 37 GHz over four convective cells in the Atlantic ITCZ as seen by TMI on June 1, 2009, around 0200Z. (Courtesy Z. Haddad, JPL/CalTech)

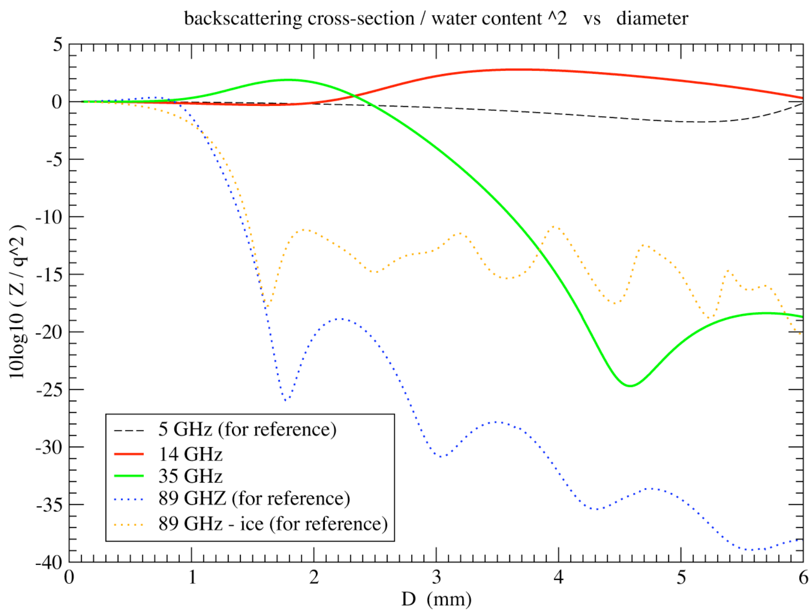

Figure 3.35: Radar signatures. Unlike the passive radiances, the radar backscattered signal does not depend on the surface temperature. In addition, the range-resolved radar returns depend on different combinations of the q' representing precipitation progressively lower in the atmosphere as the range increases, whereas the passive radiances are integrals over the entire column. Because the lightest rain consists of smaller drops, it is more reflective at Ka-band than at Ku-band; however when the Ku-band reflectivity factor exceeds a modest 27 dbZ, the Ku-band reflectivity exceeds that at Ka-band, the difference increasing with the Ku-band reflectivity. (Courtesy Z. Haddad, JPL/CalTech)

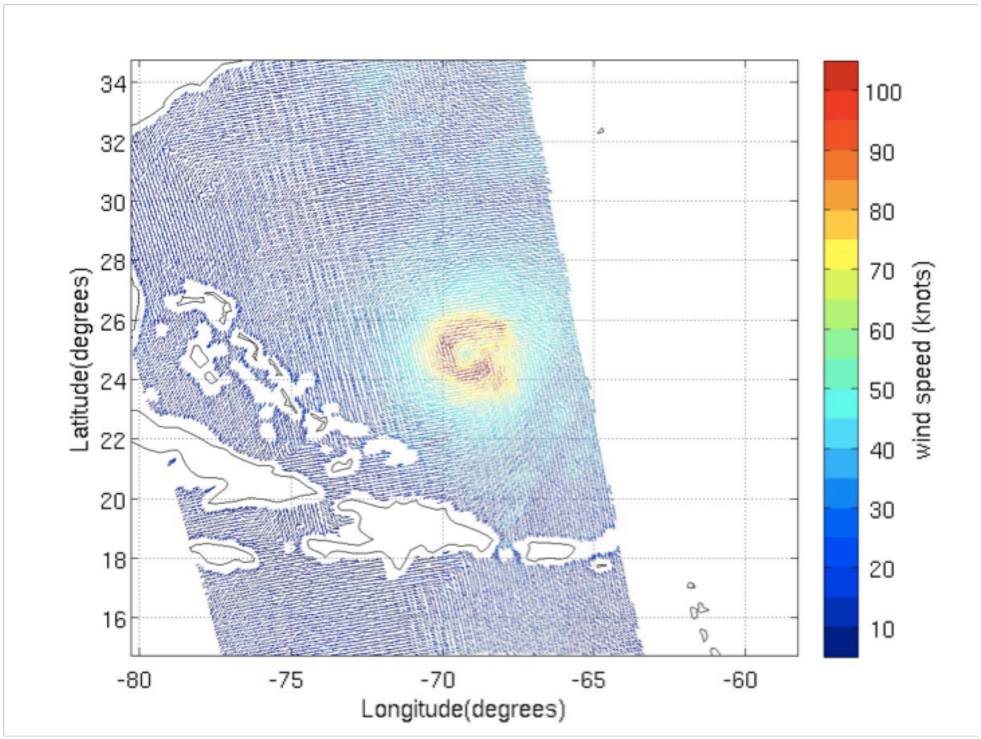

Figure 3.36: Neural network retrieved 12.5 km resolution QuikSCAT wind field of Hurricane Isabel acquired 1028 UTC on 15 September 2003. For comparison, the NHC best track maximum 1 minute sustained winds was 120 knots at 1200 UTC with storm center at 24.8 N, 69.4 W.

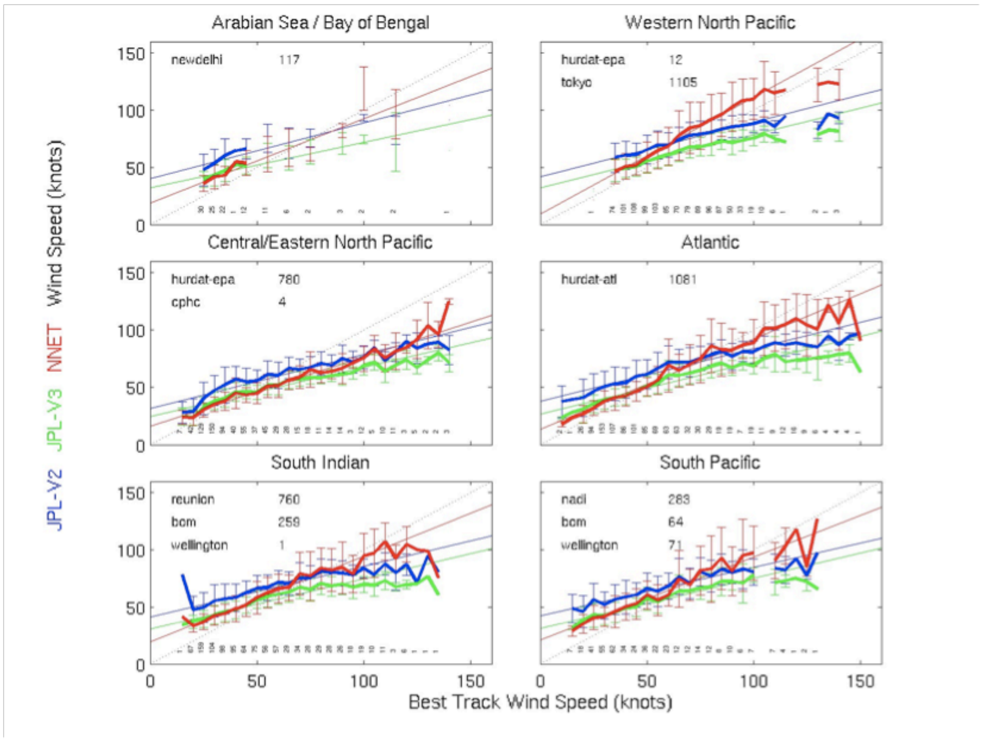

Figure 3.37: Comparison between maximum wind speeds from QuikSCAT wind fields and maximum best track 1 minute sustained wind speeds from NHC and JTWC. The red lines are hurricane neural network wind retrievals from (Stiles2012). The black dotted line is the one-to-one line. The green lines are the newly reprocessed JPL version 3 global 12.5 km winds. Version 3 makes use of a neural network for correction of wind speeds in rainy conditions (Stiles2010) that was optimized for the bulk of the global distribution of wind speeds from 0 – 40 knots. Therefore, agreement between the hurricane winds and version 3 below 40 knots is a good sign. The blue line is the currently available (version 2) JPL 12.5 km wind product. Version 2 has no correction for rain although rain is flagged. Since the comparisons shown here include all rainy and clear data, version 2 winds are biased high at low winds (due to backscatter from rain) and biased low at high winds (due to attenuation from rain and decreased sensitivity.) Statistics shown are for all named storms from October 1999 to October 2007.

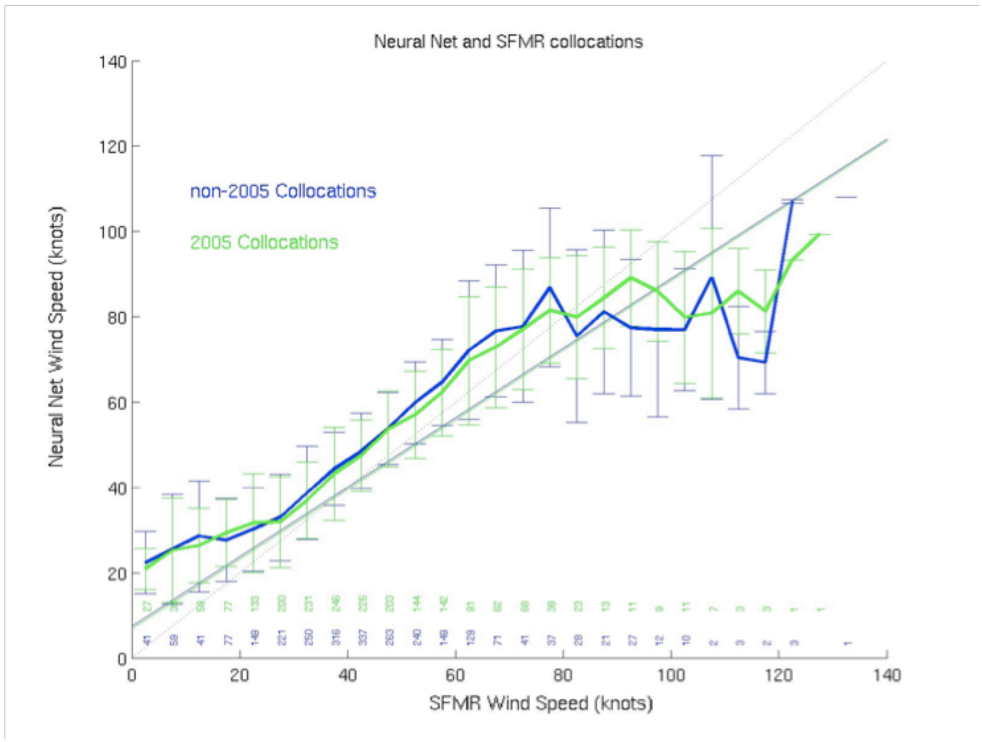

Figure 3.38: Neural Network QuikSCAT wind speeds compared with collocated SFMR aircraft overflight winds. The statistics for storms from 2005 are shown in bright green. All other years 1999-2007 inclusive are shown in blue. The solid gray line is the one-to-one line. The dark green line is a best fit line to the data. SFMR data is known to be noisy below 40 knots. From 40-80 knots the neural net winds agree well with SFMR with a small (5 knots) positive bias. Above 80 knots the agreement is worse due to insensitivity in the QuikSCAT measurements and/or poor sampling. Green and blue numbers show number of data samples.

Four

Complementary Measurements

In this section, complementary measurements that will be available during the ERM scatterometer lifetime, and their impact on helping to address the scatterometer science goals, are described. While a scatterometer system of some sort is required to provide OVW measurements, there are significant science advantages to using data that may be available at the same time as OVW measurements are collected. The largest impact would be provided by the following measurements:

4.1 Sea Surface Temperature (SST)

Coarse-resolution SST measurements, such as the ~50 km measurements provided by AMSR in near all-weather conditions, would provide significant additional information for the study of mesoscale air-sea interaction. High-resolution SST measurements, such as the ~3 km measurements provided by thermal infrared systems such as MODIS and AVHRR in clear-sky conditions, are a desirable complement to high-resolution winds, although cloud contamination makes the data difficult to use globally. Due to the persistence of SST features for times longer than a day, a 12-hour lag between the OVW and SST data collection times is acceptable. This implies that the instruments need not be collocated on the same platform, and instruments, such as AMSR, MODIS and AVHRR can be used. A future system, such as JAXA's GCOM-W1 or GCOM-W2, which will fly AMSR instruments would provide SST data globally in near all-weather conditions, albeit at coarse 50 km resolution. In addition, high-resolution measurements in clear-sky conditions with a resolution of ~3 km will be available from the AVHRR instruments on the NOAA satellites.

4.2 Ocean Color

Ocean color data, such as that provided by SeaWIFS, is indispensable for understanding the relationship between winds and ocean productivity. However, because ocean production events typically lag wind events by several days, the measurements need not be collected from the same platform to understand the effect of winds on productivity, and a 12-hour lag similar to that for SST should be sufficient to address the science questions above. A future system such as the proposed PACE mission would provide the data required for studies of physical-biological interaction from future scatterometer systems. An advantage of having winds and productivity collected at nearly coincident times (same platform or same orbit, with slight along-track shifts) would be to get a better understanding of air-sea CO2 fluxes. The flux rate depends on the wind speed, but it also depends on the partial CO2 (pCO2) pressure. Recently, the science community has come to understand the large role that can be played by ocean productivity in determining the pCO2 at the air-sea interface. Temporally coincident measurements of winds and productivity could aid in obtaining better estimates of CO2 fluxes and complement mission such as NASA's OCO-2 mission.

4.3 Precipitation and Atmospheric Attenuation/Scattering

A multi-channel microwave radiometer system, such as AMSR, can provide data to help correct for rain distortions in the scatterometer data and simultaneous estimates of precipitation. Such a combination was previously flown in the JAXA ADEOS-II mission, which carried a SeaWinds scatterometer and an AMSR instrument. The data collected by this mission demonstrated effective rain correction using the measurements from the two systems. Coincident AMSR data could mitigate the loss of the C-band channel in the DFS by providing estimates of precipitation and rain scattering that can be used to improve the scatterometer rain correction (although restrictions on high wind coverage would remain). Due to the sporadic nature of rain events, simultaneous data are required to make precipitation estimates and to flag or correct scatterometer measurements. Simultaneous data could be obtained by flying on the same platform (e.g., with AMSR on GCOM-W2) or by flying nearly coincident in time along the same orbit (e.g., on the A-train).

4.4 Complementary High-Wind Measurements

There are indications from the Aqua mission that L-band radar and radiometer data can be used to measure high winds and winds above 8 m/s. In the future, NASA's SMAP mission will contain an L-band active/passive system that could provide complementary high-wind speed data to a Ku-band scatterometer mission.

Five

White Paper Contributors

Name	**Affiliation**
Professor Mark Bourassa	Florida State University
Dr. Alexandra Chau	Jet Propulsion Laboratory/Cal Tech
Professor Dudley Chelton	Oregon State University
Dr. Michelle Gierach	Jet Propulsion Laboratory/Cal Tech
Dr. Simon Collins	Jet Propulsion Laboratory/Cal Tech
Dr. Alexander Fore	Jet Propulsion Laboratory/Cal Tech
Mr. Robert Gaston	Jet Propulsion Laboratory/Cal Tech
Dr. Ziad Haddad	Jet Propulsion Laboratory/Cal Tech
Dr. Svetla Hristova-Veleva	Jet Propulsion Laboratory/Cal Tech
Dr. Tong Lee	Jet Propulsion Laboratory/Cal Tech
Professor James McWilliams	UCLA
Dr. Larry O'Neill	Oregon State University
Dr. Dragana Perkovic	Jet Propulsion Laboratory/Cal Tech
Dr. Ernesto Rodriguez	Jet Propulsion Laboratory/Cal Tech
Dr. Yuhsyen Shen	Jet Propulsion Laboratory/Cal Tech
Dr. Bryan Stiles	Jet Propulsion Laboratory/Cal Tech
Dr. Duane Walliser	Jet Propulsion Laboratory/Cal Tech
Dr. Brent Williams	Jet Propulsion Laboratory/Cal Tech
Dr. Simon Yueh	Jet Propulsion Laboratory/Cal Tech
Professor Shang-Ping Xie	University of Hawaii
Dr. Victor Zlotnicki	Jet Propulsion Laboratory/Cal Tech

Bibliography

Babin, S., J. Carton, T. Dickey, and J. Wiggert, 2004: Satellite evidence of hurricane-induced phytoplankton blooms in an oceanic desert. *J. geophys. Res*, **109 (C3)**, C03–043.

Barton, E., et al., 1993: Supersquirt: dynamics of the gulf of tehuantepec, mexico. *Oceanography*, **6 (1)**, 23–30.

Bauer, P., 2001: Over-ocean rainfall retrieval from multisensory data of the tropical rainfall measuring mission - part I: design and evaluation of inversion databases. *Journal of Atmospheric and Oceanic Technology*, **18**, 1315–1330.

Bernie, D., E. Guilyardi, G. Madec, J. Slingo, S. Woolnough, and J. Cole, 2008: Impact of resolving the diurnal cycle in an ocean–atmosphere gcm. part 2: A diurnally coupled cgcm. *Climate dynamics*, **31 (7)**, 909–925.

Bourassa, M., et al., 2010: Remotely sensed winds and wind stresses for marine forecasting and ocean modeling. *Proceedings of the OceanObs 09: Sustained Ocean Observations and Information for Society Conference*, Venice, Italy, IOC/UNESCO and ESA, Vol. 2.

Bourassa, M. A. and K. McBeth-Ford, 2010: Uncertainty in scatterometer-derived vorticity. *Journal of Atmospheric and Oceanic Technology*, **27 (3)**, 594–603, doi:10.1175/2009JTECHO689.1.

Chelton, D., M. Freilich, and S. Esbensen, 2000: Satellite observations of the wind jets off the pacific coast of central america. part i: Case studies and statistical characteristics. *Monthly Weather Review*, **128 (7)**, 1993–2018.

Chelton, D., M. Freilich, J. Sienkiewicz, and J. Von Ahn, 2006: On the use of QuikSCAT scatterometer measurements of surface winds for marine weather prediction. *Monthly Weather Review*.

Chelton, D., P. Gaube, M. Schlax, J. Early, and R. Samelson, 2011: The influence of nonlinear mesoscale eddies on near-surface oceanic chlorophyll. *Science*, **334 (6054)**, 328–332.

Chelton, D. and S. Xie, 2010: Coupled ocean-atmosphere interaction at oceanic mesoscales. *Oceanography Magazine*.

Coppens, D., Z. Haddad, and E. Im, 2000: Estimating the uncertainty in passive-microwave rain retrievals. *Journal of Atmospheric and Oceanic Technology*, **17**, 1618–1629.

Danabasoglu, G., W. Large, J. Tribbia, P. Gent, B. Briegleb, and J. McWilliams, 2006: Diurnal coupling in the tropical oceans of ccsm3. *Journal of climate*, **19 (11)**, 2347–2365.

Delworth, T. and M. Mann, 2000: Observed and simulated multidecadal variability in the northern hemisphere. *Climate Dynamics*, **16 (9)**, 661–676.

Deser, C., A. Phillips, and M. Alexander, 2010: Twentieth century tropical sea surface temperature trends revisited. *Geophys. Res. Lett*, **37 (10)**.

Dorman, C. and C. Winant, 1995: Buoy observations of the atmosphere along the west coast of the united states, 1981-1990. *JOURNAL OF GEOPHYSICAL RESEARCH-ALL SERIES-*, **100**, 16–16.

Draper, D. and D. Long, 2004: Simultaneous wind and rain retrieval using seawinds data. *IEEE Transactions on Geoscience and Remote Sensing*, **42 (7)**, 1411–1423.

Gierach, M., M. Bourassa, P. Cunningham, J. O'Brien, and P. Reasor, 2007: Vorticity-based detection of tropical cyclogenesis. *Journal of Applied Meteorology*, **46 (8)**, 1214–1229.

Gierach, M. and B. Subrahmanyam, 2007: Satellite data analysis of the upper ocean response to hurricanes katrina and rita (2005) in the gulf of mexico. *Geoscience and Remote Sensing Letters, IEEE*, **4 (1)**, 132–136.

Gierach, M. and B. Subrahmanyam, 2008: Biophysical responses of the upper ocean to major gulf of mexico hurricanes in 2005. *J. Geophys. Res*, **113 (C4)**, C04–029.

Gille, S., S. Llewellyn Smith, and S. Lee, 2003: Measuring the sea breeze from quikscat scatterometry. *Geophysical Research Letters*, **30 (3)**.

Gille, S., S. Smith, and N. Statom, 2005: Global observations of the land breeze. *Geophys. Res. Lett*, **32 (5)**.

Gille, S., et al., 2010: Surface fluxes in high latitude regions. *Proceedings of the OceanObs 09: Sustained Ocean Observations and Information for Society Conference*, Vol. 1.

Gillett, N. and D. Thompson, 2003: Simulation of recent southern hemisphere climate change. *Science*, **302 (5643)**, 273–275.

Goes, J., H. GOMES, T. Saino, and C. Wong, 2004: Exploiting modis data for estimating sea surface nitrate from space. *Eos*, **85 (44)**.

Goes, J., T. Saino, H. Oaku, and D. Jiang, 1999: A method for estimating sea surface nitrate concentrations from remotely sensed sst and chlorophyll aa case study for the north pacific ocean using octs/adeos data. *Geoscience and Remote Sensing, IEEE Transactions on*, **37 (3)**, 1633–1644.

Haddad, Z. and K. Park, 2009: Vertical profiling of precipitation using passive microwave observations: The main impediment and a proposed solution. *Journal of Geophysical Research. D. Atmospheres*, **114**.

Haddad, Z. and K. Park, 2010: Vertical profiling of tropical precipitation using passive microwave observations and its implications regarding the crash of air france 447. *Journal of Geophysical Research*, **115 (D12)**, D12 129.

Ham, Y., J. Kug, I. Kang, F. Jin, and A. Timmermann, 2010: Impact of diurnal atmosphere–ocean coupling on tropical climate simulations using a coupled gcm. *Climate Dynamics*, **34 (6)**, 905–917.

Houze, R., 2004: Mesoscale convective systems. *Rev. Geophys*, **42 (10.1029)**.

Hu, H. and W. Liu, 2003: Oceanic thermal and biological responses to santa ana winds. *Geophys. Res. Lett*, **30 (11)**, 1596.

Jackson, D., G. Wick, and F. Robertson, 2009: Improved multisensor approach to satellite-retrieved near-surface specific humidity observations. *J. Geophys. Res*, **114**, D16 303.

Kamykowski, D., S. Zentara, J. Morrison, and A. Switzer, 2002: Dynamic global patterns of nitrate, phosphate, silicate, and iron availability and phytoplankton community composition from remote sensing data. *Global Biogeochemical Cycles*, **16 (4)**, 1077.

Lee, T., 2004: Decadal weakening of the shallow overturning circulation in the south indian ocean. *Geophysical research letters*, **31 (18)**, L18 305.

Lee, T. and W. Liu, 2005: Effects of high-frequency wind sampling on simulated mixed layer depth and upper ocean temperature. *Journal of geophysical research*, **110**, C05 002.

Lee, T. and M. McPhaden, 2008: Decadal phase change in large-scale sea level and winds in the Indo-Pacific region at the end of the 20th century. *Geophysical Research Letters*, **35 (L01605, doi:10.1029/2007GL032419)**.

Lee, T., O. Wang, W. Tang, and W. Liu, 2008: Wind stress measurements from the quikscat-seawinds scatterometer tandem mission and the impact on an ocean model. *J. Geophys. Res., C*, **12019**.

Lee, T., O. Wang, W. Tang, and W. Liu, 2009: Wind stress measurements from the quikscat-seawinds scatterometer tandem mission and the impact on an ocean model, to be published in GRL.

Li, Y. and R. E. Carbone, 2012: Excitation of rainfall over the tropical western pacific. *J. Atmos. Sci (Submitted)*.

Liang, J., J. McWilliams, and N. Gruber, 2009: High-frequency response of the ocean to mountain gap winds in the northeastern tropical pacific. *J. Geophys. Res*, **114**, C12 005.

Lin, J., et al., 2006: Tropical intraseasonal variability in 14 ipcc ar4 climate models. part i: Convective signals. *Journal of Climate*, **19 (12)**, 2665–2690.

Liu, W., W. Tang, X. Xie, R. Navalgund, and K. Xu, 2008: Power density of ocean surface wind from international scatterometer tandem missions. *International Journal of Remote Sensing*, **29 (21)**, 6109–6116.

Mahrt, L., D. Vickers, and E. Moore, 2004: Flow adjustments across sea-surface temperature changes. *Boundary-layer meteorology*, **111 (3)**, 553–564.

Mantua, N., S. Hare, Y. Zhang, J. Wallace, R. Francis, et al., 1997: A pacific interdecadal climate oscillation with impacts on salmon production. *Bulletin of the American Meteorological Society*, **78 (6)**, 1069–1080.

McClain, C., J. Christian, S. Signorini, M. Lewis, I. Asanuma, D. Turk, and C. Dupouy-Douchement, 2002: Satellite ocean-color observations of the tropical pacific ocean. *Deep Sea Research Part II: Topical Studies in Oceanography*, **49 (13-14)**, 2533–2560.

Miura, H., M. Satoh, T. Nasuno, A. Noda, and K. Oouchi, 2007: A madden-julian oscillation event realistically simulated by a global cloud-resolving model. *Science*, **318 (5857)**, 1763–1765.

Moore, G. and I. Renfrew, 2005: Tip jets and barrier winds: A quikscat climatology of high wind speed events around greenland. *Journal of Climate*, **18 (18)**, 3713–3725.

Morey, S., S. Baig, M. Bourassa, D. Dukhovskoy, and J. O'Brien, 2006: Remote forcing contribution to storm-induced sea level rise during hurricane dennis. *Geophysical research letters*, **33 (19)**, L19 603.

Nakazawa, T., 1988: Tropical super clusters within intraseasonal variations over the western pacific. *Journal of the Meteorological Society of Japan*, **66 (6)**, 823–839.

National Research Council, 2007: *Earth Science and Applications from Space: National Imperatives for the Next Decade and Beyond*. The National Academies Press, Washington D.C.

Nelson, N., N. Bates, D. Siegel, and A. Michaels, 2001: Spatial variability of the co2 sink in the sargasso sea. *Deep-sea research. Part II, Topical studies in oceanography*, **48 (8-9)**, 1801–1821.

Olsen, A., J. Trinanes, and R. Wanninkhof, 2004: Sea-air flux of co2 in the caribbean sea estimated using in situ and remote sensing data. *Remote Sensing of Environment*, **89 (3)**, 309–325.

O'Neill, L., D. Chelton, and S. Esbensen, 2012: Covariability of surface wind and stress responses to sea-surface temperature fronts. *Journal of Climate (Submitted)*.

Owen, M. and D. Long, 2011: Simultaneous wind and rain estimation for quikscat at ultra-high resolution. *Geoscience and Remote Sensing, IEEE Transactions on*, **49 (6)**, 1865–1878.

Polvani, L., D. Waugh, G. Correa, and S. Son, 2011: Stratospheric ozone depletion: The main driver of twentieth-century atmospheric circulation changes in the southern hemisphere. *Journal of Climate*, **24 (3)**, 795–812.

Roberts, J., C. Clayson, F. Robertson, and D. Jackson, 2009: Predicting near-surface characteristics from ssm/i using neural networks with a first guess approach. *J. Geophys. Res.*

Rodriguez-Rubio, E. and J. Stuardo, 2002: Variability of photosynthetic pigments in the colombian pacific ocean and its relationship with the wind field using adeos-i data. *Journal of Earth System Science*, **111 (3)**, 227–236.

Small, R. J., et al., 2008: Air-sea interaction over ocean fronts and eddies. ELSEVIER SCIENCE BV, PO BOX 211, 1000 AE AMSTERDAM, NETHERLANDS, dynamics of Atmospheres and Oceans, 274-319 pp., doi:DOI10.1016/j.dynatmoce.2008.01.001, dynamics of Atmospheres and Oceans.

Stephens, M., G. Samuels, D. Olson, R. Fine, and T. Takahashi, 1995: Sea-air flux of co2 in the north pacific using shipboard and satellite data. *Journal of Geophysical Research*, **100 (C7)**, 13 571–13.

Stramma, L., P. Cornillon, and J. Price, 1986: Satellite observations of sea surface cooling by hurricanes. *Journal of Geophysical Research*, **91 (C4)**, 5031–5035.

Tokinaga, H., S. Xie, A. Timmermann, S. McGregor, T. Ogata, H. Kubota, and Y. Okumura, 2012: Regional patterns of tropical indo-pacific climate change: Evidence of the walker circulation weakening. *J. Climate*.

Vecchi, G., A. Clement, and B. Soden, 2008: Examining the tropical pacific's response to global warming. *Eos*, **89 (9)**, 81–83.

Vecchi, G. and B. Soden, 2007: Global warming and the weakening of the tropical circulation. *Journal of Climate*, **20 (17)**, 4316–4340.

Wanninkhof, R., A. Olsen, and J. Triñanes, 2007: Air-sea co2 fluxes in the caribbean sea from 2002-2004. *Journal of Marine Systems*, **66 (1-4)**, 272–284.

Xie, S., C. Deser, G. Vecchi, J. Ma, H. Teng, and A. Wittenberg, 2010: Global warming pattern formation: Sea surface temperature and rainfall*. *Journal of Climate*, **23 (4)**, 966–986.

Xie, S., H. Xu, W. Kessler, and M. Nonaka, 2005a: Air–sea interaction over the eastern pacific warm pool: Gap winds, thermocline dome, and atmospheric convection. *Journal of Climate*, **18 (1)**, 5–20.

Xie, S., H. Xu, W. Kessler, and M. Nonaka, 2005b: Air-sea interaction over the Eastern Pacific warm pool; gap thermocline dome, and atmospheric convection. *Journal of Climate*, **18 (1)**, 5–20.

Yang, Y., S. Xie, and J. Hafner, 2008: Cloud patterns lee of hawaii island: A synthesis of satellite observations and numerical simulation. *J. Geophys. Res*, **113**, D15 126.

Zuidema, P., 2003: Convective clouds over the bay of bengal. *Monthly weather review*, **131 (5)**, 780–798.